Petroleum Science 21 (2024) 1829–1851

Contents lists available at ScienceDirect

Petroleum Science

journal homepage: www.keaipublishing.com/en/journals/petroleum-science

Original Paper

Mechanisms of fracture propagation from multi-cluster using a phase field based HMD coupling model in fractured reservoir

Yun-Jin Wang [a], Bo Wang [b, *], Hang Su [c], Tu Chang [c], Ren-Cheng Dong [d], Li-Zhe Li [a], Wei-Yu Tang [a], Ting-Xue Jiang [e], Fu-Jian Zhou [a, **]

[a] State Key Laboratory of Petroleum Resources and Engineering, China University of Petroleum-Beijing, Beijing, 102249, China
[b] China University of Petroleum-Beijing at Karamay, Karamay, 834000, Xinjiang, China
[c] China National Oil and Gas Exploration and Development Corporation Ltd., Beijing, 100034, China
[d] University of Texas at Austin, United States
[e] SINOPEC Research Institute of Petroleum Engineering, Beijing, 100101, China

ARTICLE INFO

Article history:
Received 14 October 2023
Received in revised form
7 January 2024
Accepted 8 January 2024
Available online 9 January 2024

Edited by Yan-Hua Sun

Keywords:
HMD coupling
Phase field
Natural fracture
Flow distribution
Hydraulic fracturing
Inter-fracture interference

ABSTRACT

Natural fractures (NFs) are common in shale and tight reservoirs, where staged multi-cluster fracturing of horizontal wells is a prevalent technique for reservoir stimulation. While NFs and stress interference are recognized as significant factors affecting hydraulic fracture (HF) propagation, the combined influence of these factors remains poorly understood. To address this knowledge gap, a novel coupled hydro-mechanical-damage (HMD) model based on the phase field method is developed to investigate the propagation of multi-cluster HFs in fractured reservoirs. The comprehensive energy functional and control functions are established, while incorporating dynamic fluid distribution between multiple perforation clusters and refined changes in rock mechanical parameters during hydraulic fracturing. The HMD coupled multi-cluster HF propagation model investigates various scenarios, including single HF and single NF, reservoir heterogeneity, single HF and NF clusters, and multi-cluster HFs with NF clusters. The results show that the HMD coupling model can accurately capture the impact of approach angle (θ), stress difference and cementation strength on the interaction of HF and NF. The criterion of the open and cross zones is not fixed. The NF angle (α) is not a decisive parameter to discriminate the interaction. According to the relationship between approach angle (θ) and NF angle (α), the contact relationship of HF can be divided into three categories ($\theta = \alpha$, $\theta < \alpha$, and $\theta > \alpha$). The connected NF can increase the complexity of HF by inducing it to form branch fracture, resulting in a fractal dimension of HF as high as 2.1280 at angles of $\pm 45°$. Inter-fracture interference from the heel to the toe of HF shows the phenomenon of no, strong and weak interference. Interestingly, under the influence of NFs, distant HFs from the injection can become dominant fractures. However, as α gradually increases, inter-fracture stress interference becomes the primary factor influencing HF propagation, gradually superseding the dominance of NF induced fractures.

1. Introduction

The exploration and exploitation of unconventional oil and gas resources prioritize shale and tight reservoirs, where natural fractures (NFs) commonly occur (Zhuang et al., 2020; Su et al., 2022). Achieving enhanced productivity in these reservoirs necessitates the application of horizontal well staged multi-cluster fracturing technology, a pivotal aspect of the shale gas revolution (Wang Y. et al., 2023b). While hydraulic fracturing research has extensively examined NFs and stress interference as critical factors (Tang et al., 2023; Wang Y. et al., 2023a), the current body of literature tends to compartmentalize these studies. Consequently, the synergistic impact of NFs and stress interference on fracture propagation is frequently overlooked.

In recent years, the interaction between natural fractures (NFs)

* Corresponding author.
** Corresponding author.
E-mail addresses: wangbo@cupk.edu.cn (B. Wang), zhoufj@cup.edu.cn (F.-J. Zhou).

https://doi.org/10.1016/j.petsci.2024.01.007

and hydraulic fractures (HFs) has emerged as a focal point in research. Field experiments have provided evidence that HFs can traverse NFs directly without altering their propagation direction, and they can also exhibit interruption or propagation along NFs (Zou et al., 2016a; Tang and Sheng, 2022). To elucidate the mechanisms governing the interaction between HFs and NFs, scholars have proposed various theoretical criteria. Warpinski and Teufel (1987) introduced a criterion for assessing the interaction between HFs and weak surfaces based on field experimental data, in conjunction with the Moore-Cullen criterion. However, this criterion lacked critical conditions due to its experimental determination. Addressing this limitation, Renshaw and Pollard (1995) established an interaction criterion for HF and orthogonal NFs grounded in linear elastic fracture mechanics, treating NFs as frictional interfaces. Gu and Weng (2010) extended this criterion to non-orthogonal conditions. Additionally, Guo et al. (2015) simulated the interaction of HFs and NFs using the cohesive zone method (CZM), eliminating the need for a predefined interaction criterion. Dahi-Taleghani and Olson (2011) introduced an interaction criterion for HFs and NFs, considering the cementation strength of NFs based on the critical energy release rate. Conclusively, supported by experimental results and numerical simulations, the consensus now acknowledges that reservoir physical properties, horizontal stress differences, NF properties, and stimulation parameters are the primary determinants of HF and NF interaction (Zou et al., 2016c; Dong et al., 2021). Factors such as a smaller horizontal stress difference, reduced approach angle, and weaker cementation strength have been identified as conditions inducing NF damage and prompting HF propagation along NFs (Xu et al., 2023; Zou et al., 2023).

Researchers are increasingly recognizing and emphasizing the significance of stress interference in staged multi-cluster fracturing. HFs in close proximity to each other will squeeze the surrounding reservoir during the propagation process and change the reservoir stress state, forming a stress shadow (Tan et al., 2019). This stress shadow can lead to offsetting during the HF propagation process, resulting in a larger deflection angle and, at times, fracture furcation (Huang et al., 2023). The dynamic alteration of ground stress during the multi-cluster HF propagation dynamically influences the distribution ratio of flow between perforation clusters, causing non-uniform propagation (Li et al., 2021). To effectively alleviate this stress disturbance, conditions such as a small horizontal stress difference, high pumping rate, and staggered stage arrangements have been identified (Liu et al., 2023). For traditional models like PKN, KGD, and pseudo-3D, designed for HF propagation, the HFs are relatively independent and unsuitable for addressing the complexities of multi-fracture propagation (Siriwardane and Layne, 1991; Mack et al., 1992). To overcome this limitation, Wu and Olson (2014) introduced a multi-fracture simultaneous propagation model for horizontal well staged multi-cluster fracturing using the displacement discontinuity method (DDM). They analyzed the geometry of HF and the role of stress interference. Building upon this work, Wu and Olson (2016) enhanced the model, considering the dynamic flow distribution of fracturing fluid among perforation clusters. They concluded that stress interference influences flow distribution, thereby promoting the propagation of outer fractures while inhibiting inner fractures. The cohesive zone method (CZM), incorporating nonlinear mechanical characteristics, proves effective not only for studying multi-cluster fracture propagation but also for simulating HF and NF interactions (Li et al., 2022). Nevertheless, the presetting of HF propagation paths and inaccuracies in describing approach angles between HF and NF are notable limitations. The extended finite element method (XFEM) accurately addresses non-uniform HF propagation through units describing multi-cluster HFs. However, challenges arise in handling dynamic fluid distribution and interactions with NFs due to mesh property characteristics (Hu et al., 2023), resulting in unstable calculations. The discrete fracture network (DFN) model, while simple and user-friendly for studying HF and NF interactions, is less applicable to the investigation of fracture propagation under stress interference (Wang J. et al., 2023). Particularly, addressing the competing propagation problem of multi-cluster HFs necessitates significant development and optimization on a larger scale (Hosseini et al., 2021). The displacement discontinuity method (DDM), with its simple mathematical form, is advantageous for dealing with complex fracture networks and fractures with different shapes and geometrical parameters. However, it exhibits poor accuracy in handling heterogeneous problems and lacks convergence (Jamaloei, 2021). The phase field method (PFM), capable of automatically capturing complex fracture patterns without tracking the fracture surface, is used to characterize HF propagation in indoor experiments or small scales due to computational convergence limitations and method imperfections (Zhou et al., 2020). Lepillier et al. (2020) developed a variational phase-field method using OpenGeoSys to study HF propagation in fractured reservoirs at large scales, there is still room for improvement in analyzing the competing propagation of multi-cluster HF and the dynamic changes in the stress shadow. In summary, addressing the dynamic distribution of flow, the large-scale multi-cluster HF propagation in fractured reservoirs remains a pressing challenge.

To clarify the mechanism of multi-cluster HF propagation in fractured reservoirs, the energy functional and control function in hydraulic fracturing are deduced and established based on the PFM in this study. The dynamic distribution of fluid between multiple perforation clusters is coupled, and the change of rock mechanics parameters in the process of HF propagation is improved. Finally, the HMD coupled HF propagation model is established. The coupled HMD model successfully solves the problem that the PFM is limited to small scales, does not need to specifically introduce the criterion of interaction between HF and NF, and has good applicability to the dynamic changes of stress shadow and flow rate between perforation cluster. Based on this model, the propagation mechanism of HF under single HF and single NF, reservoir heterogeneity, single HF and NF clusters, multi-cluster HFs and NF clusters are studied.

2. Mathematical model

2.1. Energy function

Fig. 1 illustrates the alterations in the reservoir corresponding parameters pre and post-fracturing. The elastic region is designated by Ω, while the external and internal discontinuity boundaries after fracturing are referred to $\partial\Omega$ and Γ, respectively. It is presumed that the porous medium exhibits homogeneity and isotropy, housing compressible and viscous fluids within its pores. $u(x, t)$ is the displacement field at position x and time t. The initial stress field σ_0, the initial displacement field u_0 and the initial fluid pressure p_0 manifest as a result of the cumulative effects of depositional and tectonic processes within the formation. Throughout the hydraulic fracturing procedure, the fracturing fluid is pumped into the reservoir to squeeze the rock at a higher pressure than the formation fracture pressure, inducing the generation of relative stress σ, relative displacement u and relative fluid pressure p. The post-fracturing stress, displacement and fluid pressure are $\sigma_0 + \sigma$, $\mu_0 + \mu$, and $p_0 + p$, respectively.

Disregarding the influence of bulk force on the energy, the energy functional of fracture initiation and propagation during hydraulic fracturing can be written as (Zhou et al., 2018)

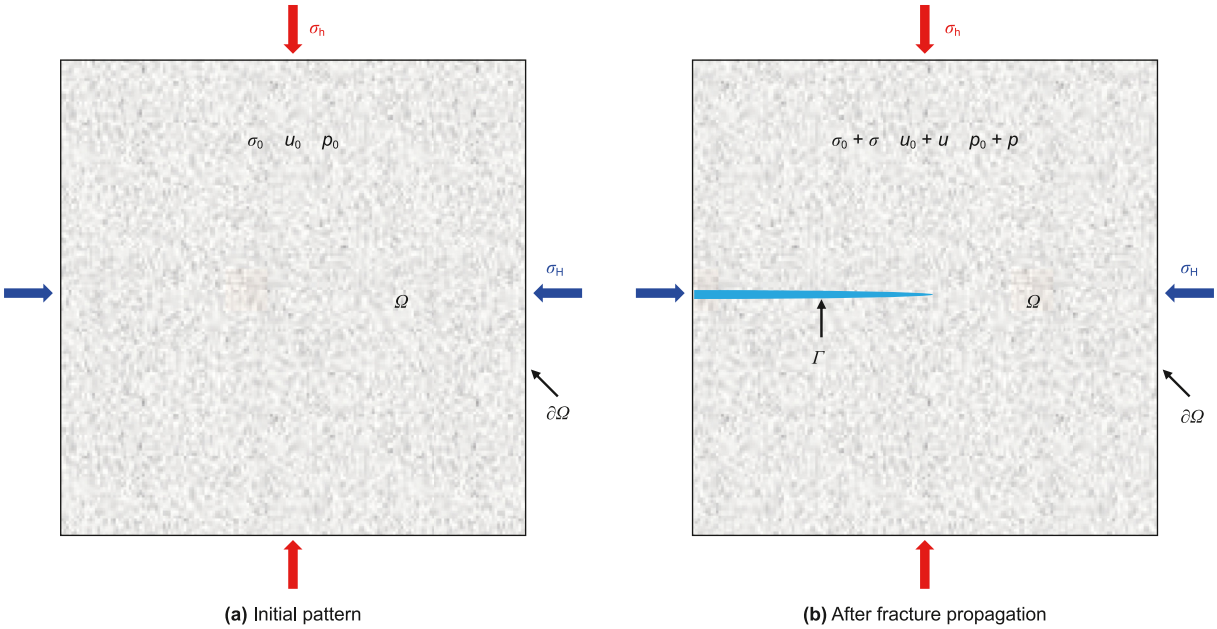

(a) Initial pattern **(b)** After fracture propagation

Fig. 1. Reservoir changes induced by fracture propagation.

$$\Psi(u,p,\Gamma)=\int_{\Omega\backslash\Gamma}\psi_\varepsilon(\varepsilon)\mathrm{d}\Omega-\int_\Omega B_\mathrm{i}\cdot p\cdot(\nabla\cdot u)\mathrm{d}\Omega+\int_\Gamma G_\mathrm{c}\mathrm{d}\Gamma-\int_{\partial\Omega_t}f_\mathrm{t}\cdot u\mathrm{d}S \tag{1}$$

where $\psi_\varepsilon(\varepsilon)$ is the elastic strain energy density, J/m^3; B_i is the Biot coefficient; G_c is the critical energy release rate, N/m; and f_t is the traction force on the boundary, N.

The initial ground stress within the reservoir during hydraulic fracturing constitutes a pivotal parameter exerting influence on both the extent and orientation of fracture propagation. It is noteworthy that fractures typically propagate in the direction of maximum horizontal principal stress. Moreover, it is observed that diminished horizontal stress difference tend to facilitate the formation of complex fracture patterns (Zhou et al., 2020). Subsequent to the inclusion of the initial stress field within the energy generalization function and its optimization, the resulting refined functional equation is presented below.

$$L(u,p,\Gamma)=\int_{\Omega\backslash\Gamma}\psi_\varepsilon(\varepsilon)\mathrm{d}\Omega+\int_{\Omega\backslash\Gamma}\sigma_0:\varepsilon\mathrm{d}\Omega-\int_\Omega B_\mathrm{i}\cdot p\cdot(\nabla\cdot u)\mathrm{d}\Omega+\int_\Gamma G_\mathrm{c}\mathrm{d}\Gamma-\int_{\partial\Omega_h}f_\mathrm{t}\cdot u\mathrm{d}S \tag{2}$$

where the first term of the equation is the elastic strain energy of the porous medium, the second term is the energy induced by the initial ground stress, the third term is the energy induced by the pore fluid, the fourth term is the fracture energy of the rock undergoing damage, and the fifth term is the external work acting on the system.

The linear strain tensor ε can be expressed as (Zou et al., 2020)

$$\varepsilon_{ij}=\frac{1}{2}\left(\frac{\partial u_i}{\partial x_j}+\frac{\partial u_j}{\partial x_i}\right) \tag{3}$$

In the context of an isotropic elastic medium, the expression for the elastic strain energy density is as follows:

$$\psi_\varepsilon(\varepsilon)=\frac{1}{2}\lambda\varepsilon_{ii}\varepsilon_{jj}+\mu\varepsilon_{ij}\varepsilon_{ij} \tag{4}$$

$$\begin{cases}\lambda=\dfrac{E\nu}{(1+\nu)(1-2\nu)}\\ \mu=\dfrac{E}{2(1+\nu)}\end{cases} \tag{5}$$

where E is the Young's modulus, GPa; ν is the Poisson's ratio; λ and μ are the Lamé coefficients.

2.2. Phase field description

The presence of HFs in the model makes it much more difficult to solve the energy functional equation using the variational approach. Therefore, the phase field ξ is used to describe the damage of the matrix and the HFs, when $\xi=0$ and $\xi=1$ indicate that the rock is undamaged and the rock is completely destroyed, respectively.

For the numerical calculation of the phase field, the form of the solution in one, two and three dimensions has been proposed by previous authors, respectively. In one dimension, the solution takes the form of an inverse exponential function (Zhang et al., 2023a). In two and three dimensions, the fracture surface density per unit volume is used to describe the phase field (Zhuang et al., 2020). Fig. 2 shows the topological structure of the abrupt and diffuse phase field in 1D scale, and the topological structure of the diffusion fractures in 2D scale in this paper. In which there is a transitional zone between complete damage and undamaged, using the theory of continuous damage mechanics, the fracture density function per unit volume can be expressed as (Miehe et al., 2010)

$$\gamma(\xi,\nabla\xi)=\frac{\xi^2}{2l_0}+\frac{l_0}{2}\nabla\xi\cdot\nabla\xi \tag{6}$$

where l_0 is the length scale parameter, m. Larger l_0 indicates lower nominal tensile strength in the phase field model. Since the length

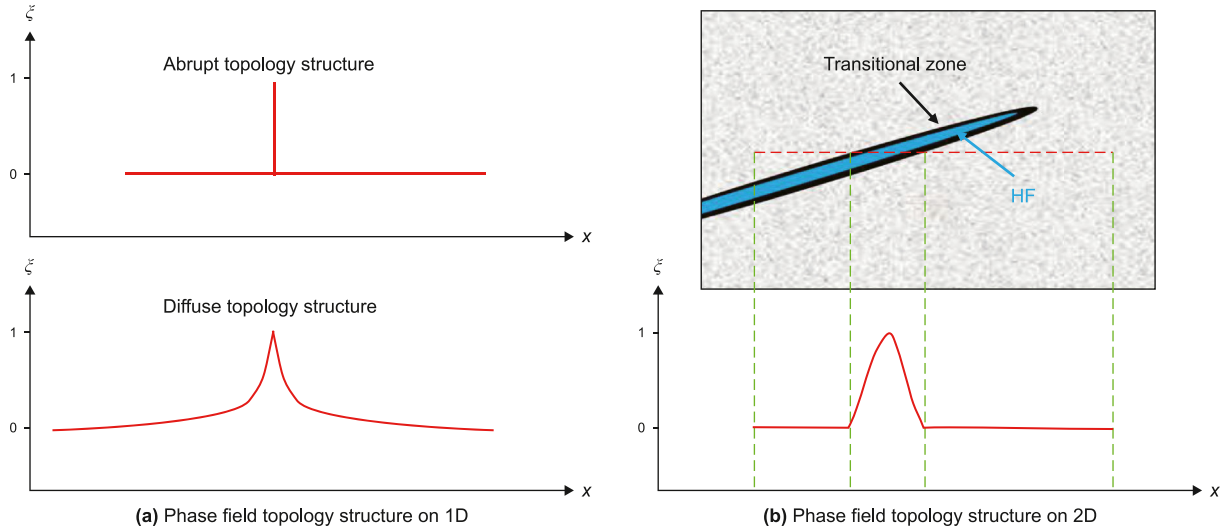

(a) Phase field topology structure on 1D (b) Phase field topology structure on 2D

Fig. 2. Topological structure of the fracture.

scale parameter l_0 is much larger than the pore size, the fracture energy in the energy functional equation can be expressed as

$$\Psi_{\mathrm{f}} = \int_{\Gamma} G_{\mathrm{c}}\,\mathrm{d}\Gamma \approx \int_{\Omega} G_{\mathrm{c}}\gamma \mathrm{d}\Omega = \int_{\Omega} G_{\mathrm{c}}\left(\frac{\xi^2}{2l_0} + \frac{l_0}{2}|\nabla\xi|^2\right)\mathrm{d}\Omega \tag{7}$$

Since in hydraulic fracturing, compressive stresses hardly cause rock damage, but the phase field formulation described above does not distinguish between fracture pattern in compression and tension. To eliminate this unrealistic fracture pattern of rock damage caused by compressive stress in the simulation, a strain spectrum decomposition is proposed by Miehe et al. (2010) to decompose the strain tensor into tensile strain tensor and compressive strain tensor.

$$\varepsilon_{\pm} = \sum_{a=1}^{d} \langle \varepsilon_a \rangle_{\pm} n_a \otimes n_a \tag{8}$$

where $\varepsilon_{\pm}$ denotes the tensile strain tensor and compressive strain tensor, respectively; ε_a and n_a are principal strains and the direction corresponding to the principal stresses; $\langle * \rangle_{\pm} = (* \pm |*|)/2$.

Bringing the decomposed strain tensor into the elastic energy density equation yields the following equation.

$$\psi_{\varepsilon}^{\pm}(\varepsilon) = \frac{\lambda}{2}\langle \mathrm{tr}(\varepsilon)\rangle_{\pm}^2 + \mu \mathrm{tr}\left(\varepsilon_{\pm}^2\right) \tag{9}$$

Consistent with the previous view (Hofacker and Miehe, 2012), this study assumes that the elastic energy density generated by compression does not affect the fracture propagation in hydraulic fracturing, then the elastic energy can be further expressed as

$$\Psi_{\varepsilon} = \int_{\Omega\setminus\Gamma} \psi_{\varepsilon}(\varepsilon)\mathrm{d}\Omega = \int_{\Omega} \left[g(\xi)\psi_{\varepsilon}^{+}(\varepsilon) + \psi_{\varepsilon}^{-}(\varepsilon)\right]\mathrm{d}\Omega \tag{10}$$

where $g(\xi)$ is the degenerate function, which is used to couple the phase field ξ and the elastic field. The degenerate function is not unique in the process of phase field solving, but needs to satisfy specific constraints of $g(0) = 0, g(1) = 0$ and $g'(1) = 0$ (Ambati et al., 2015). The degenerate function in this work is adopted as follows:

$$g(\xi) = (1-k)(1-\xi)^2 + k \tag{11}$$

where k is the stability parameter for preventing singularities.

Bringing the degenerate function into the initial stress field part of the energy functional equation, the energy function of the initial stress field can be further expressed as

$$\int_{\Omega\setminus\Gamma} \sigma_0 : \varepsilon \mathrm{d}\Omega \approx \int_{\Omega} g(\xi)\sigma_0 : \varepsilon \mathrm{d}\Omega \tag{12}$$

2.3. Governing equation for the phase field evolution

Bringing the modified fracture energy and elastic energy equations into the energy functional equation yields the following equation (Guo et al., 2018).

$$\begin{aligned} L = &\int_{\Omega} \left[g(\xi)\psi_{\varepsilon}^{+}(\varepsilon) + \psi_{\varepsilon}^{-}(\varepsilon)\right]\mathrm{d}\Omega + \int_{\Omega} g(\xi)\sigma_0 : \varepsilon \mathrm{d}\Omega \\ &- \int_{\Omega} B_{\mathrm{i}} p \cdot (\nabla \cdot u)\mathrm{d}\Omega + \int_{\Omega} G_{\mathrm{c}}\left[\frac{\xi^2}{2l_0} + \frac{l_0}{2}\nabla\xi\cdot\nabla\xi\right]\mathrm{d}\Omega - \int_{\partial\Omega_h} f_{\mathrm{t}} \cdot u \mathrm{d}S \end{aligned} \tag{13}$$

The fracture initiation and propagation are a process of minimizing the energy functional from the energy point of view, so the variation of the energy functional is set to zero using the variational method.

$$\begin{aligned} \delta L = &\int_{\partial\Omega_h} \left[\left(\sigma_{ij}^{\mathrm{e}} + g(\xi)\sigma_{0ij} - B_{\mathrm{i}} p\delta_{ij}\right)m_j - f_{\mathrm{ti}}\right]\delta u_i \mathrm{d}S \\ &- \int_{\Omega} \left(\sigma_{ij}^{\mathrm{e}} + g(\xi)\sigma_{0ij} - B_{\mathrm{i}} p\delta_{ij}\right)_j \delta u_i \mathrm{d}\Omega \\ &- \int_{\Omega} \left[g'(\xi)\left(\psi_{\varepsilon}^{+} + \sigma_{0ij}\varepsilon_{ij}\right) + \frac{G_{\mathrm{c}}\xi}{l_0}\right. \\ &\left. - G_{\mathrm{c}} l_0 \frac{\partial^2 \xi}{\partial x_i^2}\right]\delta\xi \mathrm{d}\Omega + \int_{\partial\Omega}\left(\frac{\partial\xi}{\partial x_i} m_i\right)\delta\xi \mathrm{d}S = 0 \end{aligned} \tag{14}$$

where m_j is the component of the boundary in the outward direction; $\varepsilon_{ij}^{\mathrm{e}}$ is the component of the effective stress tensor $\sigma(\varepsilon)^{\mathrm{e}}$

induced by the displacement u.

$$\sigma^{e}=g(\xi)\frac{\partial\psi_{\varepsilon}^{+}}{\partial\varepsilon}+\frac{\partial\psi_{\varepsilon}^{-}}{\partial\varepsilon}=\left[(1-k)(1-\xi)^{2}+k\right]\left[\lambda\langle\mathrm{tr}(\varepsilon)\rangle_{+}I+2\mu\varepsilon_{+}\right]+\lambda\langle\mathrm{tr}(\varepsilon)\rangle_{-}I+2\mu\varepsilon_{-} \tag{15}$$

where I is the unit tensor.

The expression of the total stress tensor can be expressed as

$$\sigma(\varepsilon)=\sigma^{e}(\varepsilon)+g(\xi)\sigma_{0}-B_{i}pI \tag{16}$$

When the phase field $\xi=1$, the rock is completely destroyed, and the region of this complete destruction is subject to a total stress of 0. The governing equation for this region can be expressed as

$$\frac{\partial\sigma_{ij}}{\partial x_{j}}=0 \tag{17}$$

The original phase field governing equation can be further expressed as

$$\left[\frac{2l_{0}(1-k)\left(\psi_{\varepsilon}^{+}+\sigma_{0i}\varepsilon_{ij}\right)}{G_{c}}+1\right]\xi-l_{0}^{2}\frac{\partial^{2}\xi}{\partial x_{i}^{2}}=\frac{2l_{0}(1-k)\left(\psi_{\varepsilon}^{+}+\sigma_{0ij}\varepsilon_{ij}\right)}{G_{c}} \tag{18}$$

The high-pressure fracturing fluid drives promote rock failure to form fractures, and matrix rock failure releases fracture energy. Even at high closure stress, the unsupported fractures may close completely. However, from perspective of energy, it is impossible for the damaged rock to be transformed into a perfect state. That is to say, the destruction of rock is an irreversible process. The fracture energy released by the destruction of the rock does not regenerate and repair the rock. Therefore, it is necessary to construct a historical field to ensure the monotonic increase of the phase field (Zhuang et al., 2020).

$$H(x,t)=\max_{s\in[0,t]}\left[\psi_{\varepsilon}^{+}(\varepsilon(x,s))+\sigma_{0}:\varepsilon(x,s)\right] \tag{19}$$

Bringing the historical field into the governing equation, the strong form of the phase field governing equation can be expressed as

$$\left[\frac{2l_{0}(1-k)H}{G_{c}}+1\right]\xi-l_{0}^{2}\frac{\partial^{2}\xi}{\partial x_{i}^{2}}=\frac{2l_{0}(1-k)H}{G_{c}} \tag{20}$$

In summary, fracture initiation and propagation are driven by the historical field H, which is physically significant as the maximum increment of the elastic energy of the porous medium in the region.

2.4. Flow field

According to the characteristics of the phase field model, the porous media can be divided into reservoir zone, transition zone, and fracture zone according to the damage degree of the rock. In this study, c_1 and c_2 are introduced as the critical values to judge the damage of the region. When the regional ξ value is less than c_1, the region is defined as the reservoir zone. When the regional ξ value is between c_1 and c_2 time, the region is defined as the transition zone. When the area ξ value is greater than c_2, the region is defined as a fracture zone. The values of c_1 and c_2 have been compared and discussed with experimental and field data (Zhou et al., 2020; Zhuang et al., 2020), and have good applicability when c_1 and c_2 are taken as 0.4 and 1, respectively. In previous studies, linear interpolation was used to characterize the variation of transition zone parameters (Shiozawa et al., 2019). In order to enhance the convergence of the model, continuous functions are used in this study for the transition zone parameters.

$$\begin{cases}\chi_{f}(\xi)=0.5+0.9375\times\left(\dfrac{2\xi-c_{2}-c_{1}}{c_{2}-c_{1}}\right)-0.625\times\left(\dfrac{2\xi-c_{2}-c_{1}}{c_{2}-c_{1}}\right)^{3}+0.1875\times\left(\dfrac{2\xi-c_{2}-c_{1}}{c_{2}-c_{1}}\right)^{5}, & c_{1}<\xi<c_{2}\\ \chi_{r}(\xi)=0.5-0.9375\times\left(\dfrac{2\xi-c_{2}-c_{1}}{c_{2}-c_{1}}\right)+0.625\times\left(\dfrac{2\xi-c_{2}-c_{1}}{c_{2}-c_{1}}\right)^{3}-0.1875\times\left(\dfrac{2\xi-c_{2}-c_{1}}{c_{2}-c_{1}}\right)^{5}, & c_{1}<\xi<c_{2}\end{cases} \tag{21}$$

The flow of fracturing fluid in the fracture and matrix is described using Darcy flow, whose continuity equation can be expressed as (Zhang et al., 2023a)

$$\rho S\frac{\partial p}{\partial t}+\nabla\cdot\left(\rho v_{f}\right)=q_{m}-\rho B_{i}\chi_{r}(\xi)\frac{\partial\varepsilon_{vol}}{\partial t} \tag{22}$$

$$v_{f}=-\frac{K_{eff}}{\mu_{eff}}\nabla p \tag{23}$$

where ρ is the density of the fracturing fluid, kg/m^3; S is the water storage coefficient, 1/Pa; v_f is the flow rate of the fluid in the fracture and porous media, m/s; ε_{vol} is the volume strain during fracturing; μ_{eff} is the effective viscosity of the fluid, Pa s; K_{eff} is the effective permeability, m^2.

The values of compression coefficient, Biot coefficient, effective viscosity, and permeability in different regions can be expressed as

$$c=\chi_{r}(\xi)c_{r}+\chi_{f}(\xi)c_{f} \tag{24}$$

$$B_{i}=\chi_{r}(\xi)B_{ir}+\chi_{f}(\xi)B_{if} \tag{25}$$

$$\mu_{eff}=\chi_{r}(\xi)\mu_{r}+\chi_{f}(\xi)\mu_{f} \tag{26}$$

$$K_{eff}=\chi_{r}(\xi)k_{r}+\chi_{f}(\xi)k_{f} \tag{27}$$

$$\phi_{p}=\chi_{r}(\xi)\phi_{r}+\chi_{f}(\xi)\phi_{f} \tag{28}$$

where c_r and c_f are the compression coefficients of the fracturing fluid in the matrix and fracture region, 1/Pa; B_{ir} and B_{if} are the Biot coefficients in the matrix and fracture region; μ_r and μ_f are the fluid viscosities in the matrix and fracture region, Pa s; ϕ_r and ϕ_f are the porosities in the matrix and fracture region; k_r and k_f are the

permeability in the matrix and fracture region, m^2.

In addition, the mechanical parameters of rocks are weakened after damage. The elastic modulus after damage can be expressed as (Wei et al., 2015)

$$E = E_0(1-\xi) \tag{29}$$

where E is the elastic modulus, GPa; E_0 is the initial elastic modulus, GPa.

The water storage coefficient S is related to porosity, compressibility, and bulk modulus and can be expressed as

$$S = \phi_p c + \frac{\left(B_i - \phi_p\right)(1-\alpha)}{K_{Vr}} \tag{30}$$

where ϕ_p is the porosity; K_{Vr} is the bulk modulus, GPa.

2.5. Dynamic distribution of fluid

Laboratory experiments and monitoring results of hydraulic fracturing treatment in the field have confirmed that the fluid intake of each perforation cluster tends to be uneven due to the competing effects of fracture propagation. Fig. 3 shows the dynamic distribution pattern of flow between multiple perforation clusters. The amount of fluid feed to the perforation cluster is determined by several influencing factors, such as wellbore friction, perforation friction, and resistance to fracture propagation. In the actual treatment process on site, these influencing factors are controlled by the injection rate, fracture propagation state, and other factors, which means that the amount of liquid entering the perforation cluster is a dynamic distribution process during the whole treatment process. According to Kirchhoff's quantification, the pressure and flow rate relationships of wellbore, perforation and fracture can be expressed as (Li et al., 2021)

$$Q = \sum_{i=1}^{N} Q_i \tag{31}$$

$$p_o = \sum_{i=1}^{N} p_{pf,i} + p_{cf,i} + p_{w,i} \tag{32}$$

where Q is the total flow rate of surface pumping, m^3/min; Q_i is the flow rate into the ith perforation cluster, m^3/min; p_o is the treatment pressure, MPa; $p_{w,i}$ is the pressure at the fracture heel in the ith perforation cluster, MPa; $p_{cf,i}$ is the wellbore pressure loss from the ith cluster to the previous cluster, MPa; $p_{pf,i}$ is the pressure loss due to perforation friction in the ith cluster, MPa.

The friction of the perforation cluster is affected by both perforation parameters and treatment parameters. Crump summarized a large amount of experimental data and established a mathematical model of the perforation cluster friction. The model is in good agreement with the field monitoring results and can be solved simultaneously with the Bernoulli equation.

$$p_{pf,i} = 0.807249\frac{\rho}{n_p^2 D_p^4 C^2} Q_i^2 \tag{33}$$

$$\Delta P - \rho g \Delta Z = K\frac{\rho Q^2}{2A^2} \tag{34}$$

where n_p is the perforation number of per perforation cluster; D_p is the perforation diameter of per perforation cluster, mm; C is the dimensionless coefficient characterizing the shape of the perforation hole.

2.6. Boundary and initial conditions

Fig. 4 shows the geometry and boundary conditions of the model. The length and width of the reservoir area of the model are L and H. There is a maximum horizontal principal stress σ_H in the x direction of the model, a minimum horizontal principal stress σ_h in the y direction, and a vertical stress σ_z in the z direction. The left and lower sides of the model are normal displacement constraints. The initial pressure of the model and the fluid pressure at the outer boundary are p_0. The fracturing fluid is injected along the wellbore at a rate of u_0 and flows into the reservoir after the perforation cluster. The parameters used in the model in this study are shown in Table 1. The model is solved using the finite element method. To effectively mitigate the effect of mesh size on fracture propagation, where the number of meshes is about 360,000.

3. Result and discussion

In order to clarify the propagation mechanism of multi-cluster HF in fractured reservoirs, this study simulates, validates, and generalizes the interaction of a single HF and a single NF using the established HMD model, and investigates the effect of heterogeneity on HF propagation. On this basis, the propagation mechanism of HF in two cases, single HF and NF cluster (density, angle, stress difference and connected fracture), and multi-cluster HFs and NF clusters (NFs, angle and connected fracture), is investigated from the scale of field stimulation.

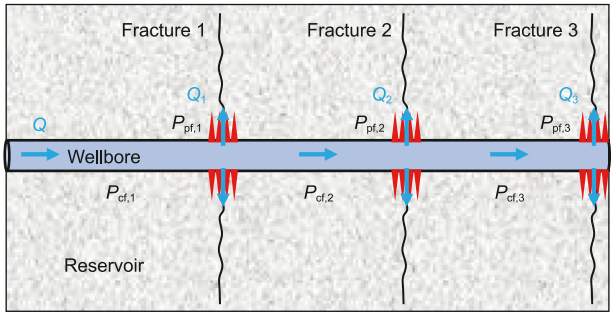

Fig. 3. Dynamic distribution model of fluid.

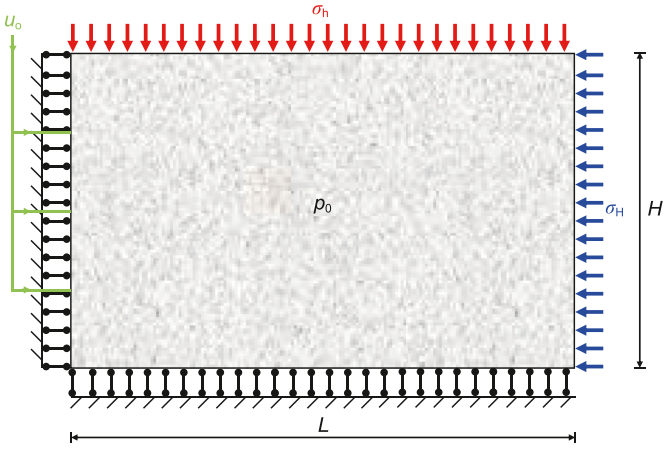

Fig. 4. Model geometry and boundary conditions.

Table 1
Parameters of the model in this study.

Parameter	Value	Parameter	Value
E_0, GPa	45	ν	0.2
G_c, N/m	5000	k	1×10^{-9}
l_0, m	0.1	c_1	0.4
c_2	1	ρ_r and ρ_f, kg/m^3	1.1×10^3
μ_r and μ_f, Pa s	0.1	c_r and c_f, 1/Pa	1×10^{-8}
k_r, m^2	1×10^{-7}	k_f, m^2	1×10^{-16}
D_p, mm	12	n_p	16
ϕ_r	0.08	ϕ_f	0.16

3.1. Interaction between HF with NF

Horizontal stress difference, approach angle, and cementation strength are important factors affecting the interaction of NF with HF (Dong R. et al., 2023). This section investigates the interaction of HF with NF under the conditions of different influencing factors. Where the injection rate is 8 m^3/min and the critical energy release rate of natural fractures is 3000 N/m, the simulation results are shown in Fig. 5. The interaction state of HF and NF can be divided into two states: open and cross. When the minimum horizontal principal stress and maximum principal stress are equal, the HF will open the relatively weak NF and propagate along it. As the horizontal stress difference continues to increase, the HF makes a gradual transition from opening to crossing the NF. This is because the greater the horizontal stress difference, the greater the resistance to activate the NF according to the distribution of the stress field around the HF during the fracturing process (Li et al., 2018). The larger the approach angle between the HF and the NF, the more difficult it is to open the NF under the combined effect of the fracture tip stress and the far site stress. The simulation results are consistent with the results of the friction interface discrimination criterion (Dahi-Taleghani et al., 2011). When the horizontal stress difference is 8 MPa and the approach angle is larger than 60°, all the HF formed cross the NF.

The interaction state of HF and NF in this simulation result is counted and compared with the previous experimental results, and the comparison results are shown in Fig. 6. Comparing the interaction state of HF and NF under different conditions, it can be seen that the simulation results have a good similarity with the previous experimental results (Li et al., 2021). According to the interaction state in the simulation results of HF and NF, they are divided into two zones, the open zone and the cross zone. It is worth noting that the open and cross zones are not random, and there is a clear criterion between the two zones. The fluid pressure in the HF can open the NF and thus divert the HF only when the low-level stress difference or approach angle is less than 60°. Conversely, the HF will cross the NF and propagate in the previous direction. Opening NF to divert HF can increase the complexity of fractures and

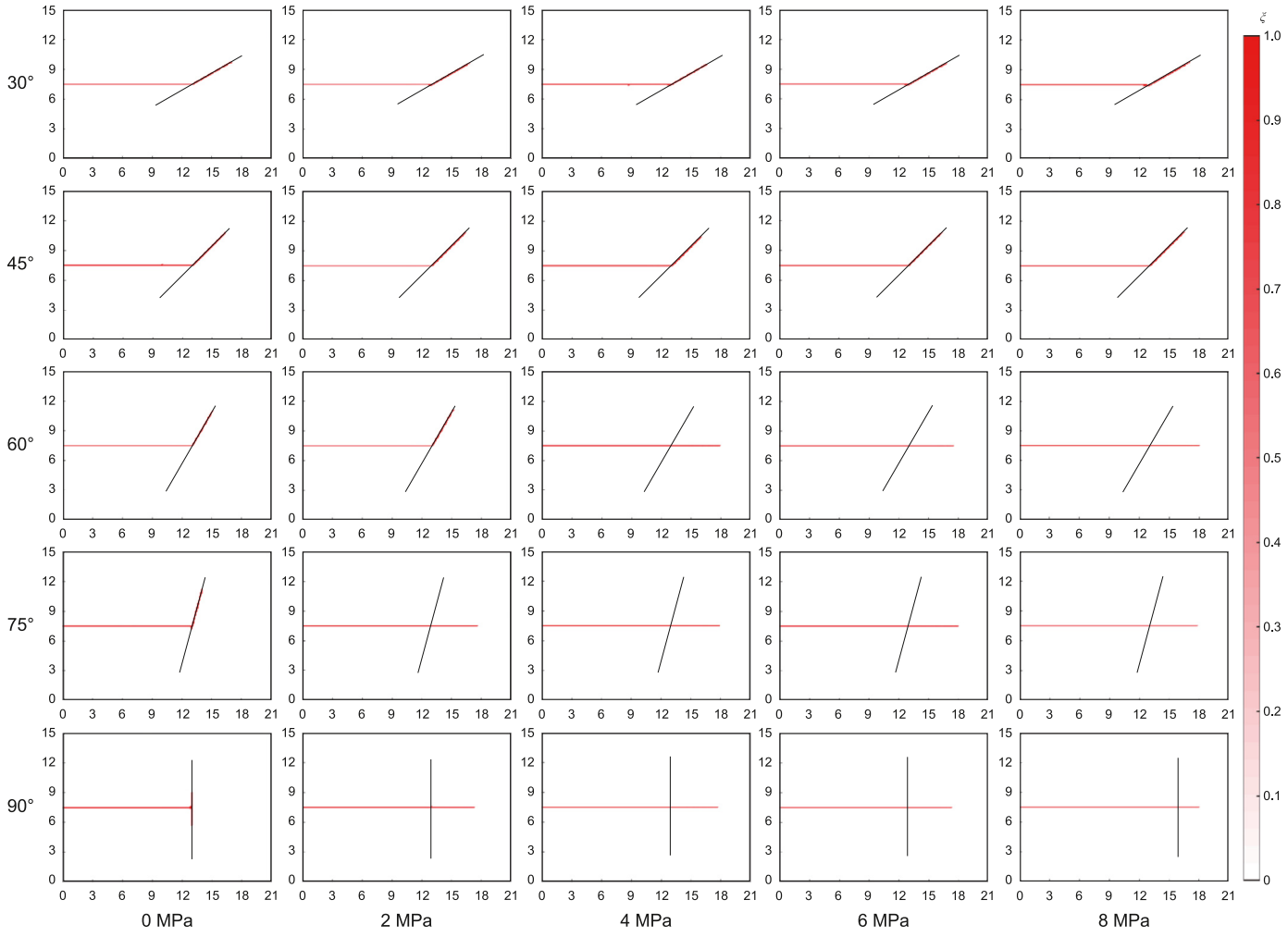

Fig. 5. HF propagation pattern under different NF states (G_c = 3000 N/m).

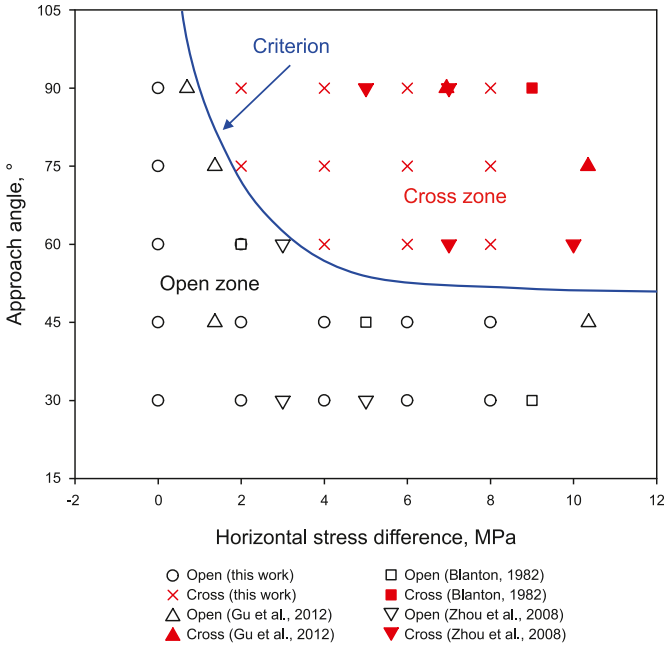

Fig. 6. Interaction patterns of HF and NF (Blanton, 1982; Gu et al., 2012; Zhou et al., 2008).

effectively improve the utilization of oil and gas reserves between fractures. Crossing through the NF and propagating in the previous direction can increase the propagation distance of the HF and effectively utilize the oil and gas reserves between the wells (Zou et al., 2020).

Actual NFs often have different cementation strengths within the fractures due to the geologic formations and depositional environments (Li et al., 2020). Figs. 7 and 8 show the interaction between HF and NF for G_c of 2000 and 4000 N/m for NF, respectively. When the cementation strength is low ($G_c = 2000$ N/m), the NF is less difficult to open. Even when the approach angle between the NF and the HF is 75°, it is still possible for the NF to be opened and for the HF to divert. On the contrary, when the cementation strength is high ($G_c = 4000$ N/m), it is relatively difficult for the NF to be activated. Even when the approach angle between the NF and the HF is 60° and the horizontal stress difference is 2 MPa, the NF still cannot be activated and opened. The interaction of HF and NF under weak and strong cementation strengths is shown in Fig. 9(a) and (b), respectively. It is obvious that the intersection of HF and NF is still characterized by a regional distribution. The overall trend remains that HF still predominantly crosses NF at higher levels of stress difference and larger approach angles. However, due to the different cementation strengths of the NF, the distribution characteristics of the interaction are slightly different.

In order to analyze the effect of the cementation strength of the NF on the HF diverting more obviously, the distribution characteristics of the criteria for the open and cross zones under different cementation strengths are plotted in Fig. 9(c), and the zones located at the upper right and lower left of each cementation strength criterion line are the cross and open zones, respectively. As the cementation strength of the NF increases, the criterion line is shifted to the lower left corner. This results in a decreasing open zone and an increasing cross zone. In the extreme, when the cementation strength is equal to the strength of the rock itself, the

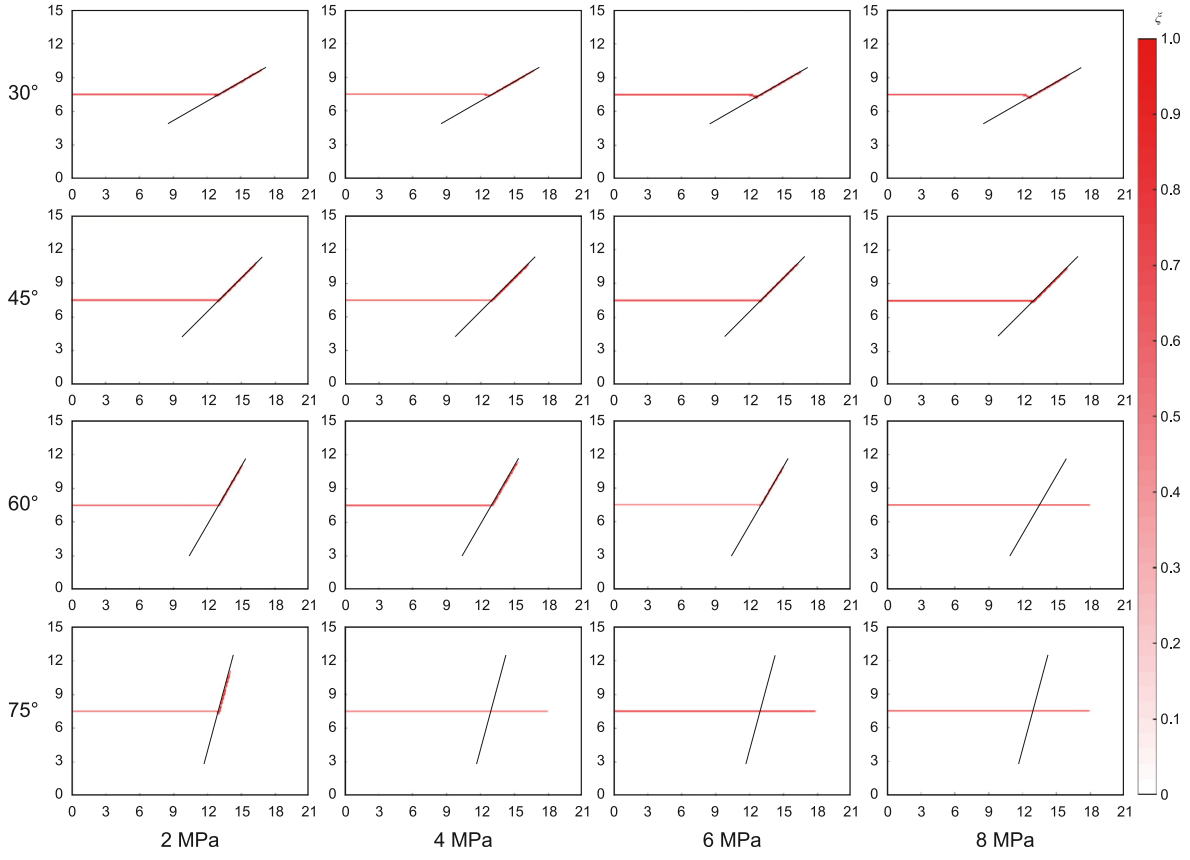

Fig. 7. HF propagation pattern under different NF states ($G_c = 2000$ N/m).

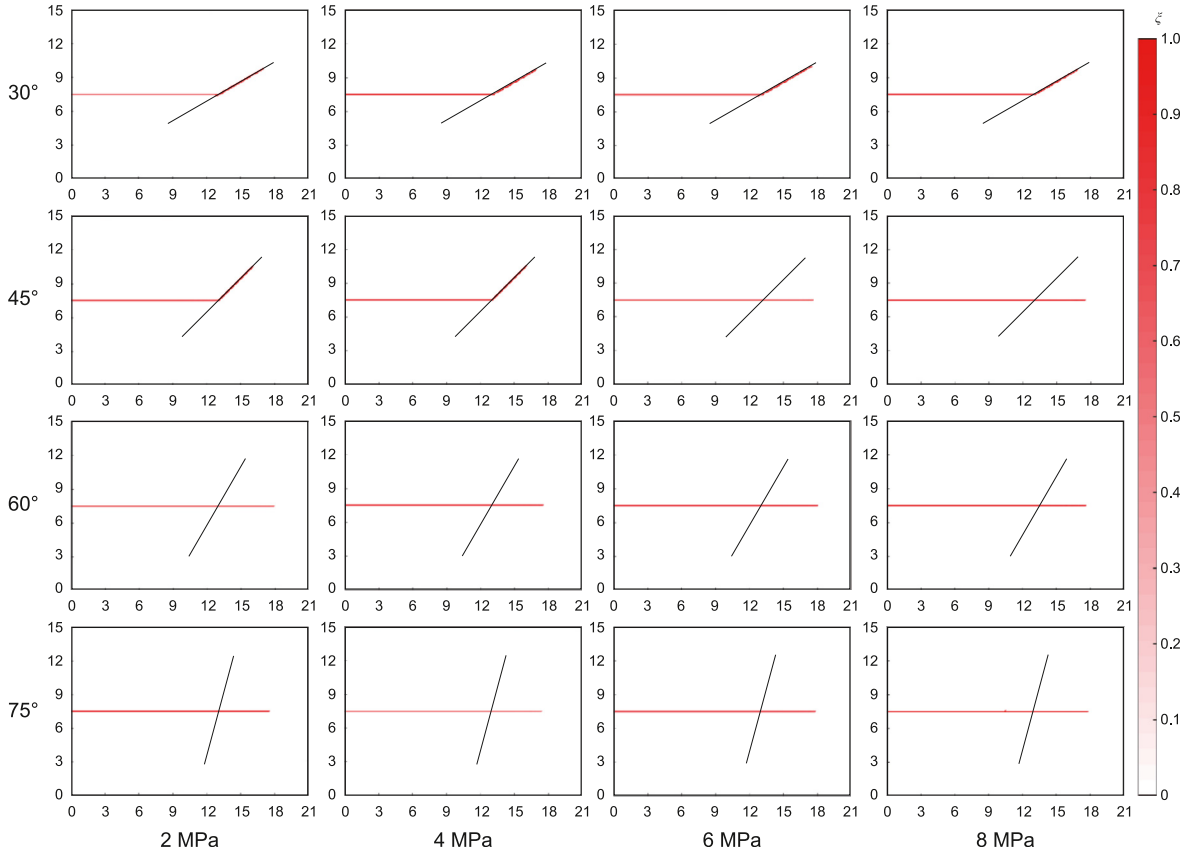

Fig. 8. HF propagation pattern under different NF states (G_c = 4000 N/m).

open zone will disappear completely. That is to say, no matter how the horizontal stress difference and approach angle change, the HF will not divert and propagate in the direction of the maximum horizontal principal stress. The simulation results are highly similar to the previous experimental results (Bahorich et al., 2012). Fig. 9(d) shows the distribution characteristics of the effective minimum horizontal principal stress (minimum horizontal principal stress—pore pressure, negative sign indicates compressive stress) when the HF interacts with the NF during the HF propagation process. During the fracturing process, the high-pressure fracturing fluid causes a localized tensile zone at the fracture tip thereby causing damage to the rock and continued fracture propagation. The fluid within the fracture continues to compress the area around the fracture wall, resulting in localized compression zones. As the HF continues to propagate, the NF opens when the tensile zone at the tip of the HF contacts the NF and the tensile principal stresses along the perpendicular to the NF interface are greater than the stresses required to open the NF. From the friction interface theory, the smaller the cementation strength of the NF, the smaller the G_c and critical principal tensile stress required along the interface perpendicular to the NF (Dahi-Taleghani et al., 2011), and the lower the difficulty of opening the NF.

3.2. Effect of heterogeneity on HF propagation

The rocks in the reservoir are composed of minerals and cements, which tend to show different degrees of heterogeneity locally under sedimentation and diagenesis (Wang Y. et al., 2023c). Weibull distribution has a better descriptive ability for this non-homogeneous feature of reservoirs (Zhang et al., 2023a), and its distribution function is shown below.

$$f(x,\lambda,m)=\begin{cases}\dfrac{k}{\lambda}\left(\dfrac{x}{\lambda}\right)^{m-1}\mathrm{e}^{-(x/\lambda)^m}, & x\geq 0\\ 0, & x<0\end{cases} \tag{35}$$

where x is a random variable; λ is a scale parameter; and m is a shape parameter. In this study, λ is the average value of variable x, and m characterizes the heterogeneity of the reservoir. Fig. 10 shows the distribution of G_c in the reservoir when m is 5, 6, 7, and 8, respectively. Among them, the smaller the m, the more dispersed the value of G_c is, which indicates the greater heterogeneity of the reservoir. Fig. 11 shows the distribution of Young's modulus and Poisson's ratio in the reservoir when m is 5.

Fig. 12 shows the propagation results of HF when the horizontal stress difference is 2 MPa. As can be seen from the figure, when the heterogeneity of the reservoir is strong (m = 5), even without the influence of NF and stress interference, the formation of the HF still exhibits a certain degree of tortuosity, and the calculated tortuosity is 1.08. As the degree of heterogeneity continues to decrease, the tortuosity of HF continues to decrease. When the heterogeneity of the reservoir is weak (m = 8), a relatively straight and simple fracture is formed, and the tortuosity is 1.03. This is due to the fact that the propagation path of the HF is determined by the stress relationship, stimulation technology and rock minerals (Zhang et al., 2023b), and the HF tends to propagate in the direction of lower energy loss. When the degree of local heterogeneity is strong, the resistance of HF propagation along different directions is quite different, which makes the propagation mode of HF more tortuous and complex. With the decreasing degree of heterogeneity, the guiding ability of reservoir minerals for HF is gradually weakened, so that the HF tends to form a simple fracture propagating along the

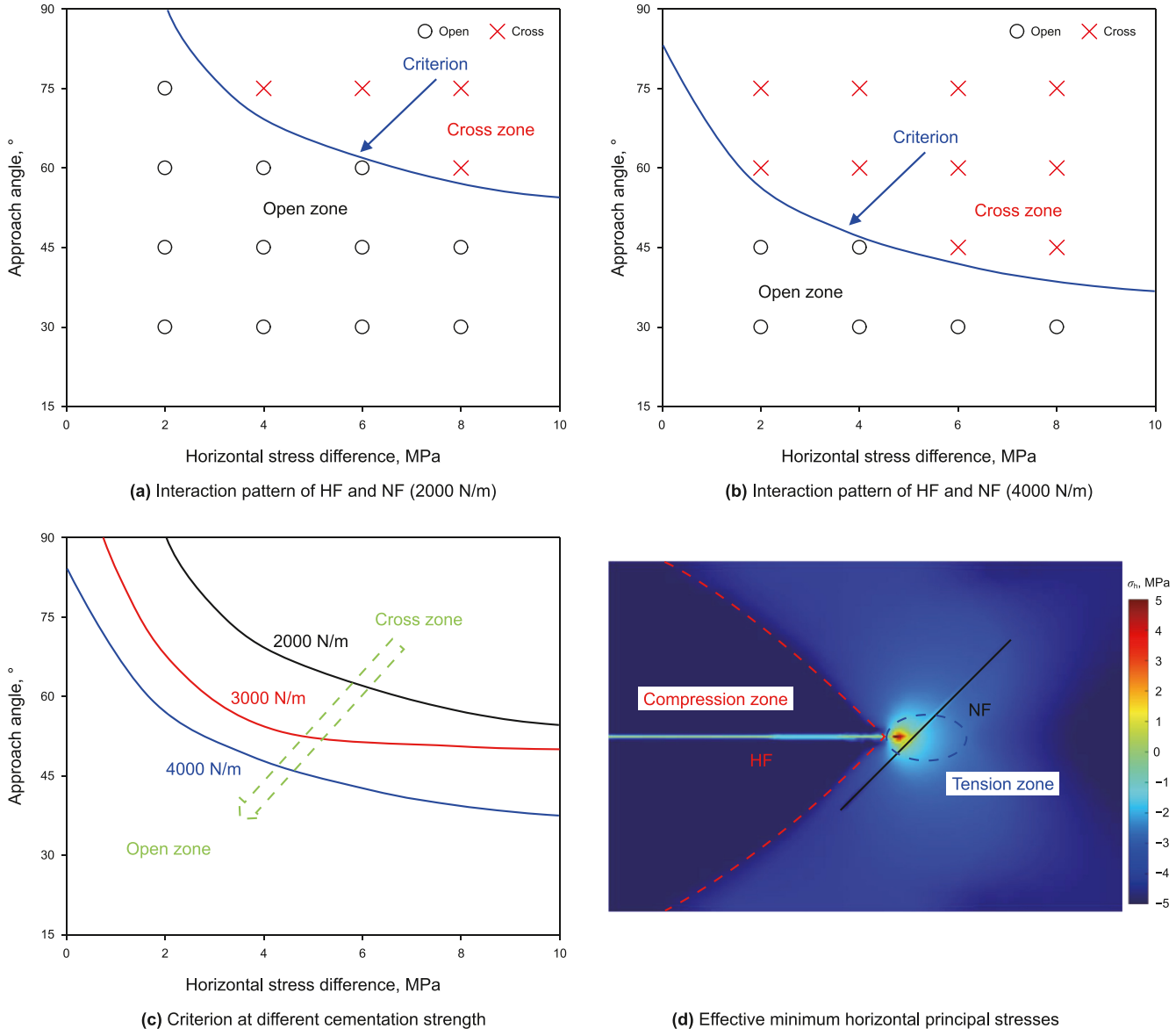

(a) Interaction pattern of HF and NF (2000 N/m)

(b) Interaction pattern of HF and NF (4000 N/m)

(c) Criterion at different cementation strength

(d) Effective minimum horizontal principal stresses

Fig. 9. Interaction and regional distribution of HF and NF.

direction of the maximum horizontal principal stress. Fig. 13 shows the propagation results of HF when the horizontal stress difference is 4 MPa. It can be observed that the tortuosity of HF also decreases with the decrease of heterogeneity. The tortuosity is 1.02 and 1.00 respectively when the degree of heterogeneity is strong ($m = 5$) and weak ($m = 8$). Fig. 14 shows the calculation results of the tortuosity degree of the HF under different degrees of heterogeneity. By comparing and analyzing the propagation results and tortuosity of HF with a horizontal stress difference of 2 and 4 MPa, it can be seen that when the horizontal stress difference is 4 MPa, the tortuosity of HF decreases significantly. That is, when the horizontal stress difference is greater than 4 MPa, other ways such as communicating NF and temporary plugging and diverting are needed to enhance the complexity of the HF. The comprehensive analysis shows that the HF propagation is more sensitive to the horizontal stress difference relative to the degree of heterogeneity. Meanwhile, for the study of HF propagation in hydraulic fracturing, considering the heterogeneity of the reservoir is often a more realistic reflection of the actual HF propagation process than assuming that the reservoir is homogeneous. Therefore, all the subsequent simulations adopt the heterogeneity reservoir as the basis of simulation.

3.3. Interaction of HF with NF clusters

Natural fractures (NFs) in reservoirs are usually formed by one or more geotectonic movements, and NFs caused by the same tectonic movement often have similar properties in terms of geometry and rock mechanics (You and Lee, 2021). This section investigates the interaction process of HF and NF clusters. The heterogeneity of the reservoir matrix is characterized using a Weibull distribution ($m = 5$). The distribution of NFs in the reservoir is mainly characterized by density, location, angle and length. In order to facilitate the study and analysis, this study assumes that the NFs are straight and the characteristic parameters of NFs are independent of each other and conform to the corresponding probability distribution functions, respectively.

According to the rock engineering description of NFs, the characteristic parameters of NFs in reservoirs are usually distributed by

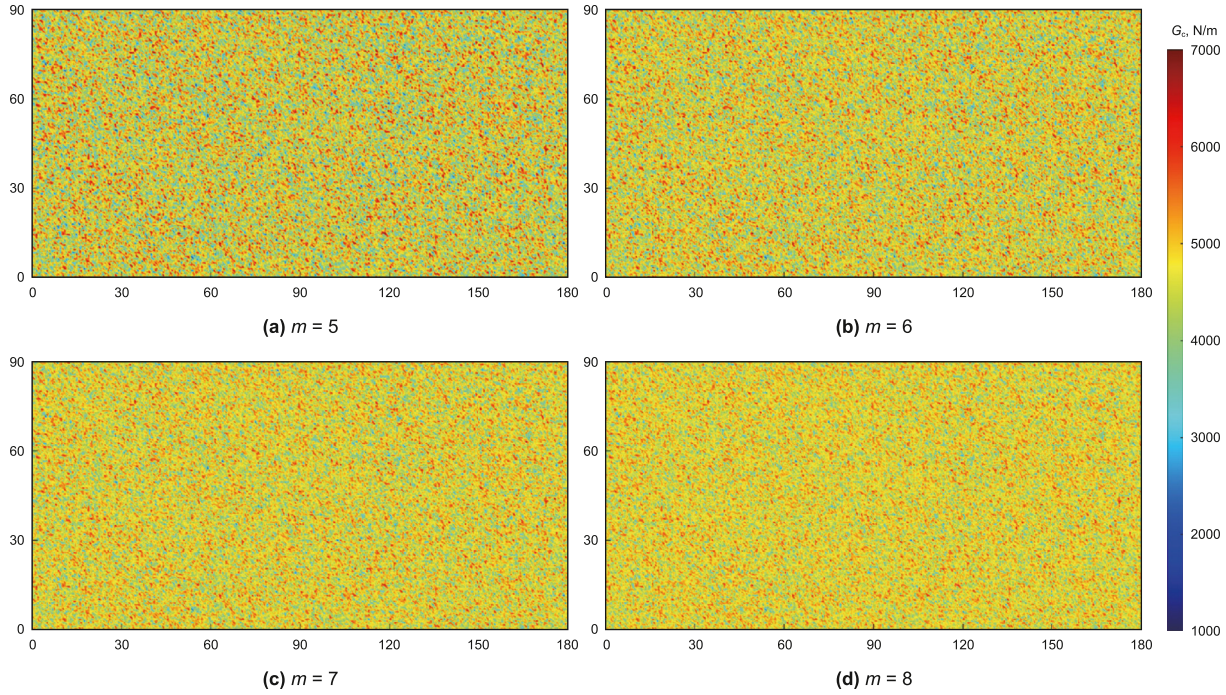

Fig. 10. Distribution of critical energy release rates in the reservoir.

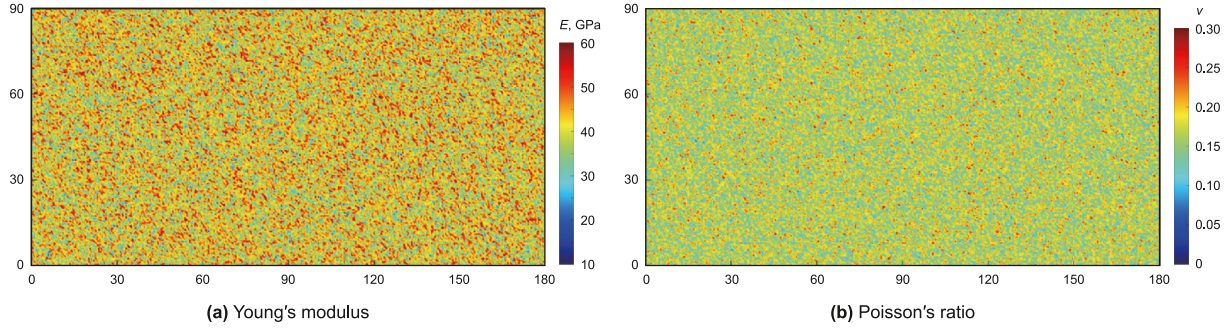

Fig. 11. Distribution of Young's modulus and Poisson's ratio in the reservoir.

several probability distributions (Wang et al., 2020). The location of the NFs usually satisfies the uniform distribution, the fracture density usually conforms to the Poisson distribution, and the fracture length conforms to the negative exponential distribution or the log-normal distribution. In this study, the uniform distribution is used for the location of NFs, the normal distribution is used for the angle of NFs, and the log-normal distribution is used for the length of NFs. The probability density functions of the various distributions are described in Table 2. The density of NFs indicates the number of NFs in the reservoir. In this study, the density of NFs is described using linear density, whose physical meaning is the length of NFs per unit area, which can be expressed by Eq. (36) (Zou et al., 2016b). Fig. 15 shows the distributions of critical energy release rate, Young's modulus, and Poisson's ratio in the reservoir for density, average fracture length, and α (average angle with the direction of maximum horizontal principal stress) of 0.1, 10 m, and 30°, respectively.

$$D_{\mathrm{frac}} = \frac{L_{\mathrm{frac}}}{A} \tag{36}$$

where D_{frac} is the linear density of the NFs, 1/m; L_{frac} is the length of the NFs, m; A is the area of the region where the NFs are located, m^2.

Density of NFs. Different scales of tectonic movements tend to generate different numbers of NFs (Peng et al., 2023). This section investigates the effect of density of NFs on the propagation pattern of HF in NF clusters. Fig. 16 shows the propagation results of HF at different densities of NFs. The average angle between the NFs and the maximum horizontal principal stress in the model is 30°, the average fracture length is 10 m, and the horizontal stress difference is 4 MPa. Fig. 16(d) demonstrates the maximum offset distance (OD_{max}) of the HF, that is, the maximum vertical distance of HF from the original fracture propagation direction. In this case, the OD_{max} of the HF is 10.85, 15.62, 17.72, and 20.71 m for densities of NFs of 0.05, 0.066, 0.083, and 0.1, respectively. This is because, when the number of NFs is small, the HF encounters fewer NFs in the propagation process, which makes the diverting effect of the NFs in the reservoir on the HF limited. With the increasing NFs density, the probability of the HF contacting the NFs in the propagation process increases gradually. When the horizontal stress difference and approach angle are located in the open zone, the higher contact probability can enhance the diverting degree of the NFs to the HF, which makes the HF deviate from the original direction of

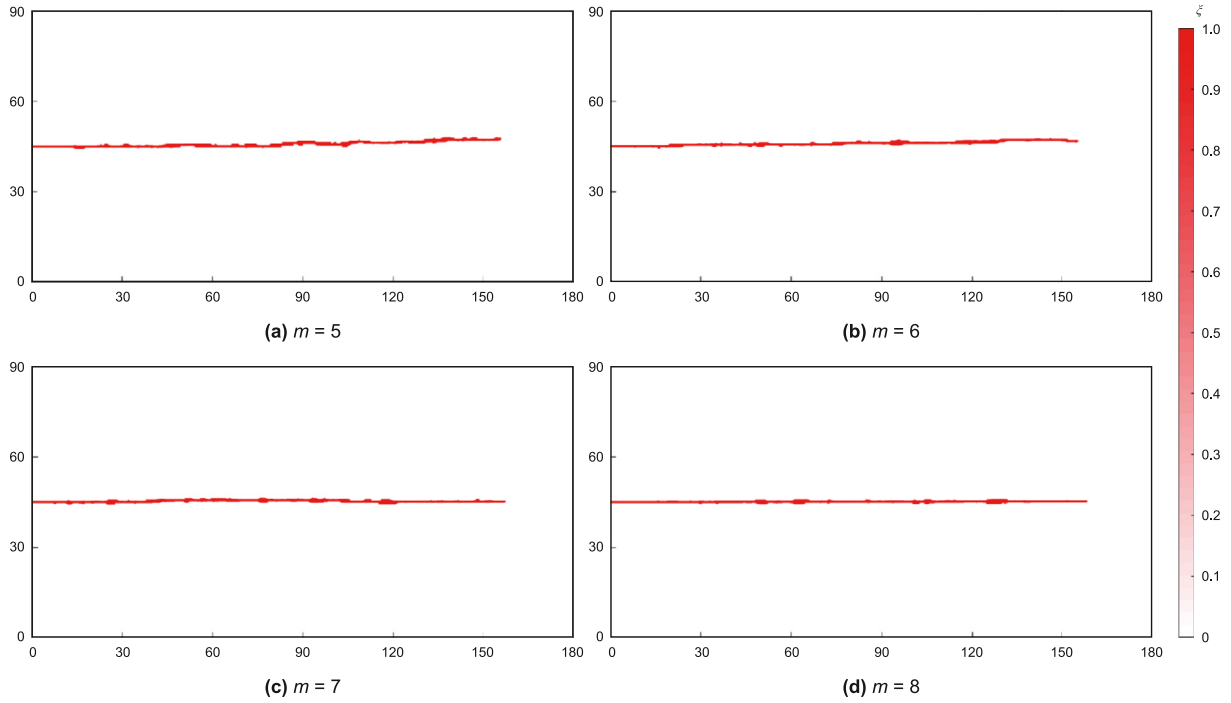

Fig. 12. The propagation mode of HF at different heterogeneity ($\Delta\sigma = 2$ MPa).

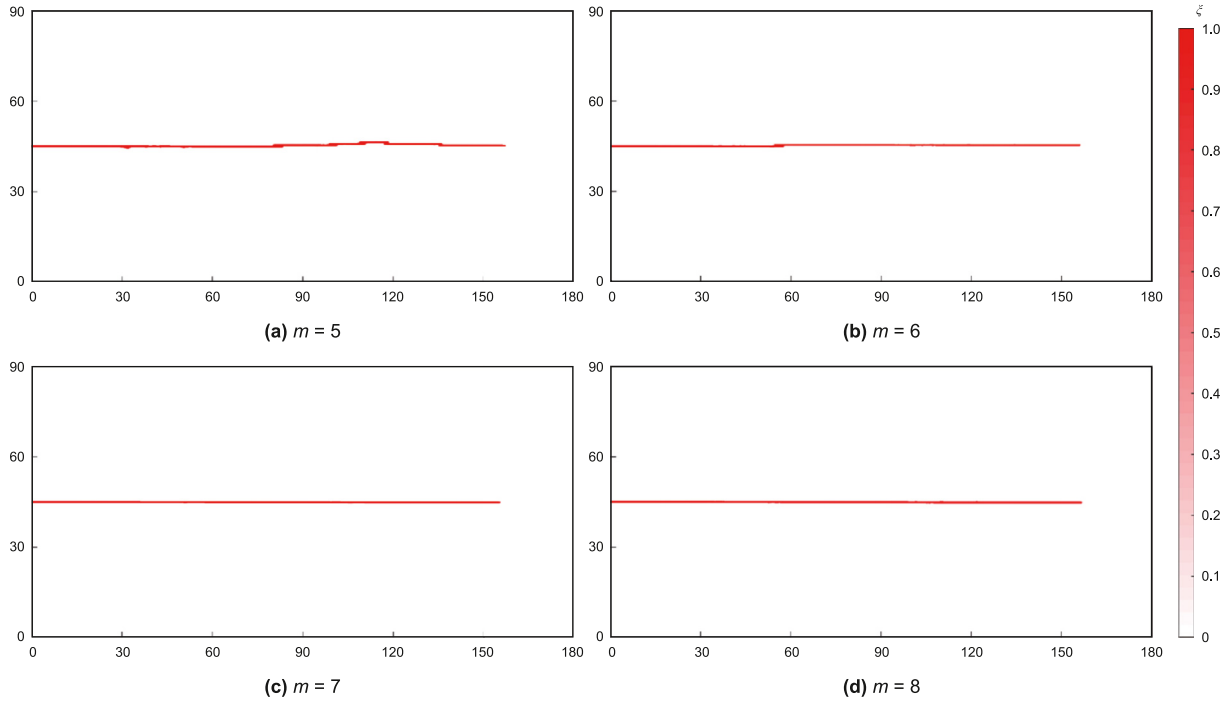

Fig. 13. The propagation mode of HF at different heterogeneity ($\Delta\sigma = 4$ MPa).

propagation. The tortuosity of HF is calculated in Fig. 17. It can be seen that the tortuosity of HF has been significantly improved. When the density of NFs is 0.1, the tortuosity reaches 1.19. The OD_{max} shows a strong correlation with the tortuosity. Overall the tortuosity of the HF also increases with the density of the NFs, but with slight local variations. The tortuosity of HF with a density of 0.083 is slightly smaller than that of HF with a density of 0.066. This is because a higher density of NFs means a higher probability that a HF will come into contact with a NF during propagation. However, if the location of the NFs does not appear in the path of HF propagation, the degree of interaction between HF and NFs remains low even though the number of NFs is higher. In general, the higher the density of NFs, the higher the probability of contact between HF and NFs, the more tortuous the morphology of HF, and the larger the OD_{max}. However, the tortuosity and the OD_{max} of HF are equally affected by the location of NFs in addition to density.

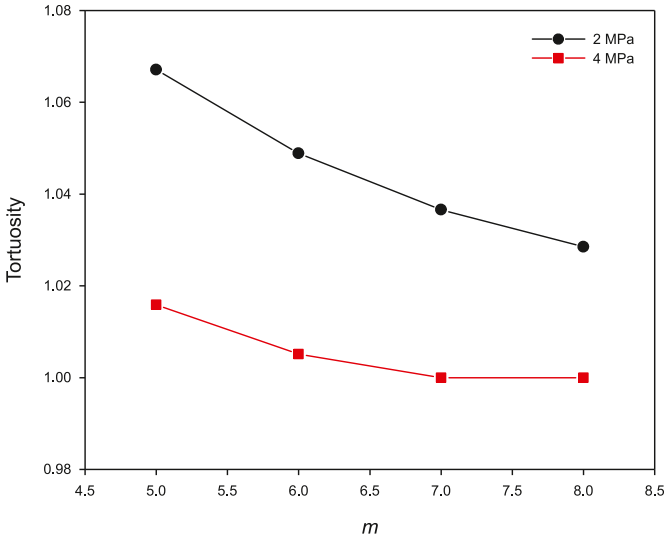

Fig. 14. The tortuosity of HF at different heterogeneity.

Angle of NFs. As the results of the above section show, the interaction between HF and a single NF is affected by the approach angle between the NF and the HF. The propagation path of HF in actual reservoirs will be more complicated due to the combined effect of heterogeneity and NF clusters on fracture propagation. This section investigates the propagation patterns of HF under heterogeneous conditions in NF clusters with different approach angles. Fig. 18 shows the propagation patterns of HF in NF clusters with different α.

It can be seen from the simulation results, similar to the simulation results of HF and a single NF, when α is low, the NF has a strong diverting performance for HF. When the average approach angle of NFs is 30°, the interaction between HF and NFs is still mainly open, and the propagation path of HF is mainly along NFs. When the average approach angle of NFs gradually increases to 45° and 60°, the interaction relationship between HF and NF clusters is more complicated than that between HF and a single NF. The interaction between HF and NF clusters is mainly open and cross two cases. There are two main reasons for this. The first reason is the critical value of the approach angle. It can be seen from the above study that the critical value of the approach angle of the interaction between HF and NF is between 45° and 60°. When the approach angle of some NFs is larger than this critical value, then the HF mainly crosses the NFs. On the contrary, the HF will open the NFs prompting the HF to divert. The second reason is the heterogeneity of the reservoir. As can be seen in Figs. 12 and 13, the heterogeneity of the reservoir can make the HF have a certain degree of tortuosity, and this degree of tortuosity can change the propagation direction of the local HF, which makes the actual approach angle (θ) between the HF and the NF change. Fig. 19 demonstrates the contact relationship between tortuous HF and NF, which can be categorized into three types ($\alpha = \theta$, $\alpha < \theta$ and $\alpha > \theta$) according to the tortuosity of HF in heterogeneity reservoirs. When $\alpha > \theta$, the actual contact angle may prompt the HF to open the NF prompting the HF to divert even though α satisfies the crossing condition. Similarly, when $\alpha < \theta$, even though α is located in the open zone, the actual contact angle may drive the HF to cross the NF to form a single HF. It is worth noting that the HF may still open along the wall of the NF after opening the NF, thus continuing to cross the NF. Due to the heterogeneity of the reservoir and the change of stress relationship during HF propagation, the HF may open and propagate along the weak side of the NF surface. The simulation results have been reported several times in previous experiments and field monitoring results (Peng et al., 2019). When α is large, the interaction relationship between HF and NF remains dominated by crossing, which is the same pattern of interaction as between HF and a single NF. This is because with larger α, the local tortuosity of the HF is not sufficient to reduce the larger approach angle between the HF and NFs below the critical approach angle, resulting in a relatively simple shape and scale of the HF.

Fig. 20 shows the calculated tortuosity and OD_{max}. As can be seen from the figure, the OD_{max} and the tortuosity still show a strong correlation. Both the OD_{max} and the tortuosity show a tendency of increasing and then decreasing with the increase of the angle between the NFs and the maximum horizontal principal stress direction. When the angle is 45°, the tortuosity and the OD_{max} reach the maximum, 1.22 and 23.13 m. When the angle is 75°, the tortuosity and the OD_{max} reach the minimum, 1.08 and 3.83 m. The overall results of the tortuosity and the OD_{max} are in good agreement with the reasons for the interactions between the HF and the NF clusters discussed above. That is, HF is mainly open to the low angle NF cluster, open and cross the middle angle NF cluster, and cross the high angle NF cluster. In addition to that, when the interaction between HF and NF clusters are both dominated by crossing, the greater the angle between HF and NFs, the greater the degree of HF offset, and the more tortuous the HF formed.

Horizontal stress difference. Horizontal stress difference is an important influencing factor that affects the interaction of HF and NFs. The larger the horizontal stress difference is, the more difficult it is for NFs to open after encountering a continuously propagating HF. This section simulates the effect of different horizontal stress differences on HF propagation in NF clusters. The average angle between the NFs and the maximum horizontal principal stress is 30°. Fig. 21 shows the propagation results of HF at horizontal stress differences of 2, 4, 6, and 8 MPa. From the simulation results, it can be seen that when the horizontal stress difference is small, due to the influence of NFs, the distance of HF offset along the original propagation direction is large. With the gradual increase of the horizontal stress difference, this degree of offset shows a trend of gradual decrease. Fig. 22 shows the calculated tortuosity and

Table 2
Probability density function and parameter description.

Distribution	Probability density function	Parameter
Uniform distribution	$f(x) = \begin{cases} \frac{1}{2a}, & \bar{x}-a \le x \le \bar{x}+a \\ 0, & \text{others} \end{cases}$	a: Maximum deviation $\bar{x}$: Average
Normal distribution	$f(x) = \frac{1}{\sigma\sqrt{2\pi}} e^{-\frac{(x-\mu)^2}{2\sigma^2}}$	μ: Average σ: Standard deviation
log-normal distribution	$f(x) = \frac{1}{x \lg \sigma\sqrt{2\pi}} e^{\frac{(\lg x-\mu)^2}{2\sigma^2}}$	μ: Average σ: Standard deviation

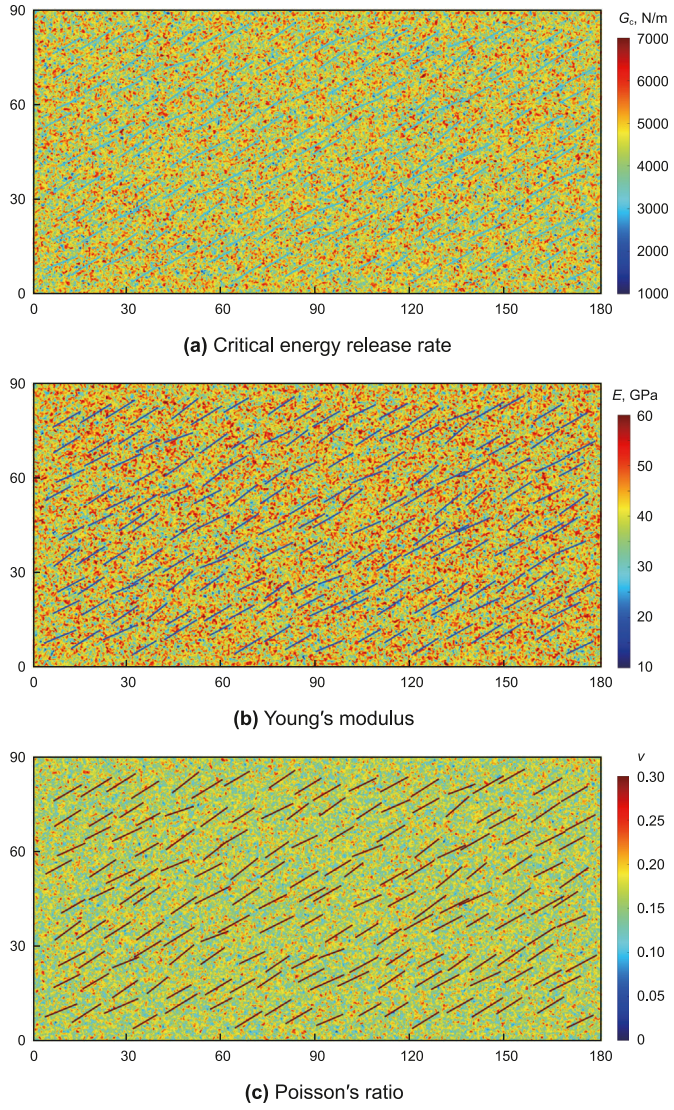

Fig. 15. Distribution of mechanical parameters containing NFs in reservoirs.

OD_{max}, and it is obvious that the tortuosity and OD_{max} of HF still show a strong positive correlation. When the horizontal stress difference is 2 MPa, the tortuosity and the OD_{max} are 1.24 and 37.88 m, respectively. With the increasing of the horizontal stress difference, the tortuosity and the OD_{max} show a tendency of decreasing gradually. When the horizontal stress difference is 8 MPa, the tortuosity and the OD_{max} decrease to 1.13 and 13.92 m, respectively. Similar to the simulation results of the HF interacting with a single NF, the main interaction between the HF and the NF clusters is still dominated by the opening in this condition. However, the diverting effect of NF clusters on HF is slightly different under different horizontal stress differences.

A comparative analysis of the HF in the blue circle in Fig. 21 shows that the HF will open and propagate along the NF after contacting the NF. After propagating out of the NF, if there is no weak surface on the NF wall, the HF will propagate along the tip of the NF. Fig. 23 shows a schematic diagram of a HF breaking through at the tip of the NF after propagating along the NF. The stress difference relationship in the figure is $\Delta\sigma_0 = 0 < \Delta\sigma_1 < \Delta\sigma_2 < \Delta\sigma_3$. Obviously, when the horizontal stress difference is $\Delta\sigma_0$, the HF will continue to propagating along the direction of the NF. On the contrary, if there is a horizontal stress difference, the propagation direction of HF will be deflected in the direction of the maximum horizontal principal stress under the influence of the ground stress field. According to the mechanical calculation of rock damage in hydraulic fracturing, the magnitude of the deflection is related to the size of the horizontal stress difference (Jiang and Younis, 2016). The larger the horizontal stress difference is, the larger the magnitude of deflection is. Because of the "corrective" effect of the horizontal stress difference, the HF continues to propagate in the direction of the maximum horizontal principal stress. The larger the horizontal stress difference is, the stronger this "corrective" effect is, which is finally reflected in the smaller OD_{max} and tortuosity of HF.

Connected NFs. The NFs in the NF clusters in the above study are almost one type, with almost the same direction and more discrete distribution. The actual formation usually undergoes several tectonic movements, and these NFs can be categorized according to their directions and mechanical characteristics (Dong S. et al., 2023). NFs with different angles can intersect to form connected fractures. This section comparatively investigates the effect of connected NFs on HF propagation. The values of α are 30° and 45° in the cases of disconnected NFs and ±30° and ±45° in the cases of connected NFs. The linear density of NFs in both cases is 0.1 and the horizontal stress difference is 4 MPa. The simulation results are shown in Fig. 24. Due to the condition of this stress difference and angle, the NF cluster has a strong guiding effect on HF propagation. However, there are two groups of NF clusters with opposite directions in the case of the connected NFs, which happen to play a complementary role to the HF and greatly reduce the OD_{max}. It is worth noting that the conclusion that the HF is positively correlated with the OD_{max} and tortuosity of the disconnected NF clusters is no longer applicable here. This is because in the case of the connected NFs, the HF is ultimately barely deflected, but the HF is clearly tortuous and complex. More importantly, in the case of the connected NFs, branch fractures are formed during the HF propagation. The HF at the intersection of the connected NFs is selected for force analysis (Fig. 25). When the HF propagates to the intersection of the connected NFs, in the combined stress field formed by the tensile stress generated at the HF tip and the far-field stress, the tensile stresses superimposed along the vertical direction of the NF wall are $\sigma_{\alpha 1y}$ and $\sigma_{\alpha 2y}$, respectively. When the difference between α_1 and α_2 is small, the difference between $\sigma_{\alpha 1y}$ and $\sigma_{\alpha 2y}$ provided by the combined stress field is also small. At this time, the HF is able to open these two sets of NFs at the same time, resulting in branch fractures.

For HF with branch fractures, the tortuosity is difficult to calculate, while the fractal dimension is more applicable to describe this complexity. Therefore, in this study, the fractal dimension is calculated for disconnected and connected NFs, and the results are shown in Fig. 26. As can be seen from the figure, the good linear relationship verifies the feasibility of the fractal dimension for describing the complexity of HF. The fractal dimensions of NF clusters with average angles of 30°, 45°, ±30°, and ±45° are 2.0879, 2.0952, 2.1019 and 2.1280, respectively. Comparison of the results of the connected and disconnected NFs shows that the complexity of HF in the case of connected NFs is significantly higher than that in the case of disconnected NFs. The existence of branch fractures significantly enhances the complexity of HF and stimulating reservoir volume. Meanwhile, similar to the simulation results of disconnected NFs, the HF formed by a natural fracture angle of ±45° is more complex than that formed by a natural fracture angle of ±30° in the case of connected natural fractures. The reason for this

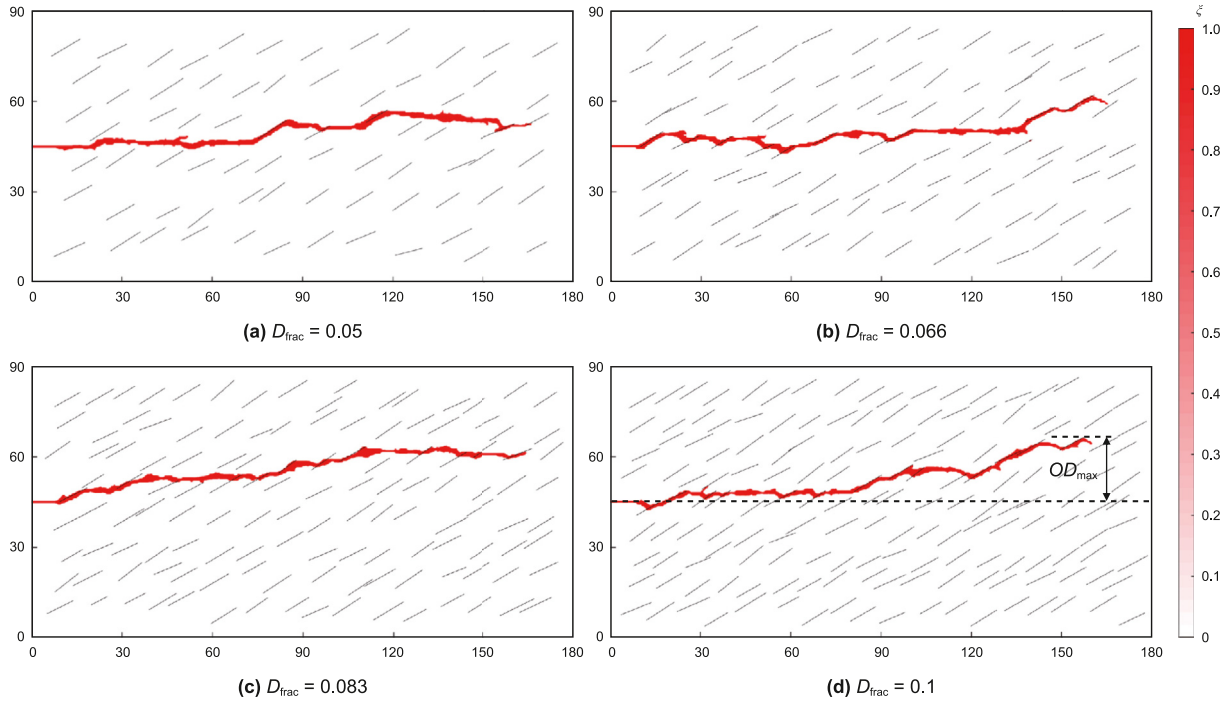

Fig. 16. The results of HF propagation at different densities of NFs.

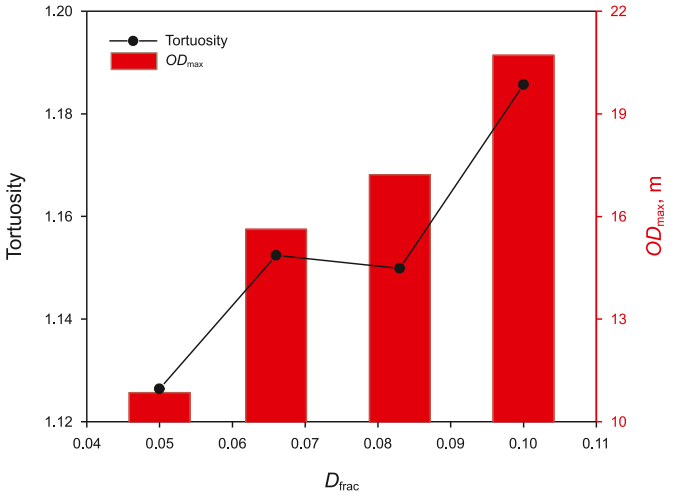

Fig. 17. Tortuosity and OD_{max} of HF at different NFs density.

is the same as the guiding effect of NFs on HF propagation in the case of disconnected NFs. Overall, compared with disconnected NFs, connected NFs can promote the formation of branch fractures during HF propagation, which is an important factor in the formation of complex fracture networks.

3.4. Interaction of multi-cluster HF with NF clusters

Multiple perforation clusters are usually fractured at the same time during the hydraulic fracturing process, and the HF generated by different perforation clusters usually have different offset and propagation patterns due to stress interference. In fractured reservoirs, the fracture propagation of multiple perforation clusters not only needs to consider the interaction between HF and NF, but also needs to consider the stress interference between hydraulic fractures during the propagation process, and the propagation pattern is more complicated than that of a single HF. This section comparatively analyzes the mechanism of multi-cluster HF propagation in NF clusters, and also investigates the effects of NF angles and connected NFs on HF propagation of multiple perforation clusters. The reservoir parameters are consistent with Table 1. There are three perforation clusters in the model, the spacing of perforation clusters is 22.5 m, and the horizontal stress difference is 6 MPa. To further prevent HFs from breaching the boundary and thus affecting the simulation results, the upper and lower boundaries of the study area are extended by 30 m each.

NFs. The interaction results of HF and NF clusters show that the NF clusters are able to guide the HF propagation to some extent, which makes the HF deviate from the original propagation direction. This section simulates and compares the effect of NF clusters on the HF propagation of the three perforation clusters, and the simulation results are shown in Fig. 27. Fig. 27(a) shows the propagation pattern of multi-cluster HFs in the absence of NF clusters. At the early stage of HF propagation, the HFs of all three perforation clusters show a straight propagation trend due to the small interference between HFs. With the gradual propagation of the HFs, the stress shadows cannot be ignored gradually, resulting in the outer HF1 and HF3 to be offset to the outer side, whose OD_{max} are 9.98 and −11.16 m, respectively (assuming that the downward offset is negative). The inner HF2 is more difficult to propagate under the extrusion of the outer HFs, and it hardly undergoes offset and the propagation distance is smaller than that of the outer HFs. When the HFs propagate to a certain distance, the gap between the propagation distance of the inner HF and the outer HFs gradually increases. At this time, the inner HF has almost no interference effect on the outer HFs, and only the outer HFs influence each other. The tendency to cause the outer HFs to deflect outward is alleviated to a certain extent. In the extreme case that the inner HF2 propagates very short or even not under strong stress interference, then there has been only the mutual interference of the outer HFs during the HFs propagation. Therefore, the phenomenon of no

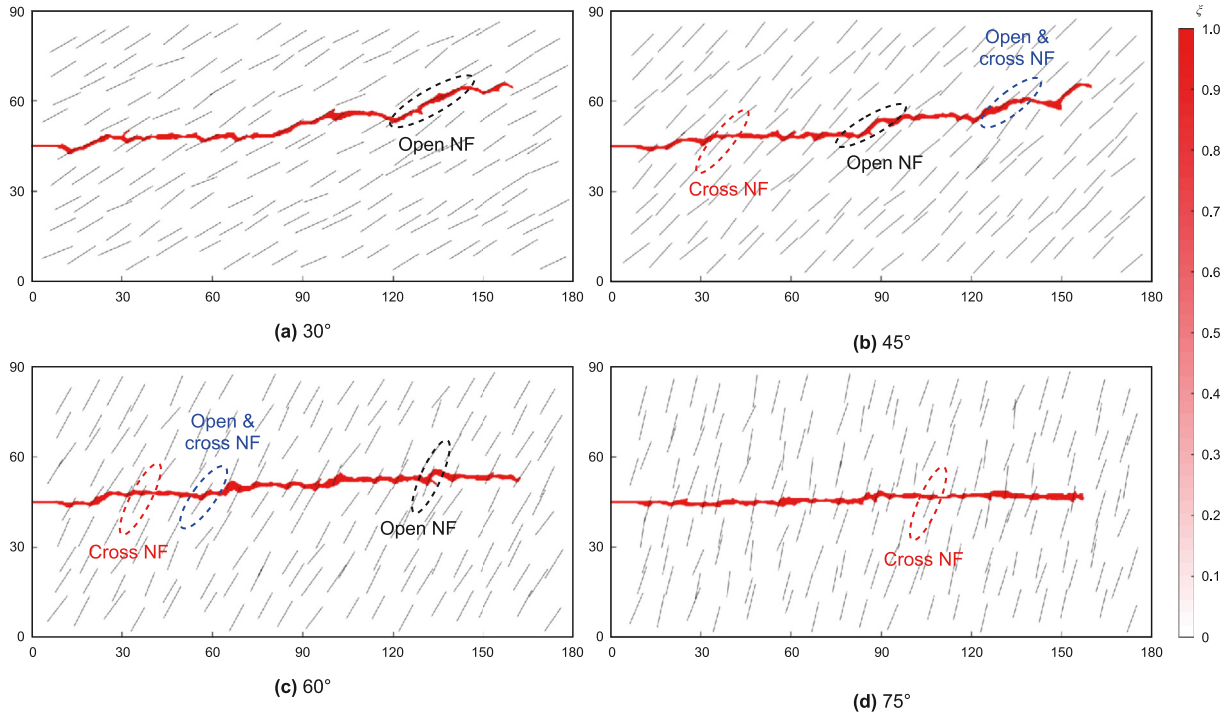

Fig. 18. The results of HF propagation at different angles of NFs.

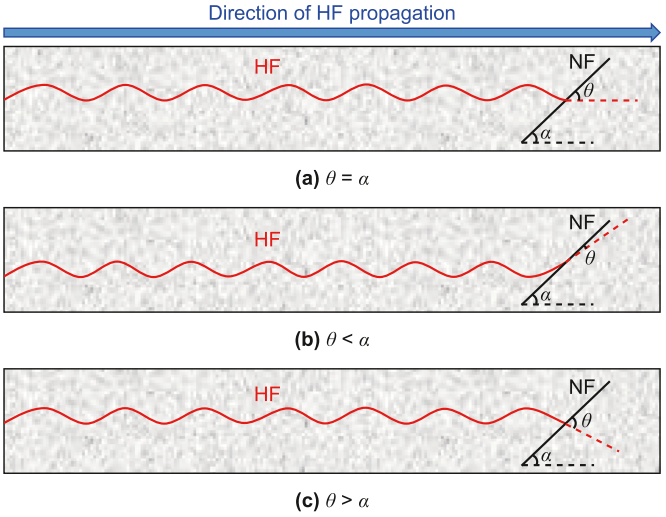

Fig. 19. Relationship between the angle of NFs and the approach angle between NFs and HF.

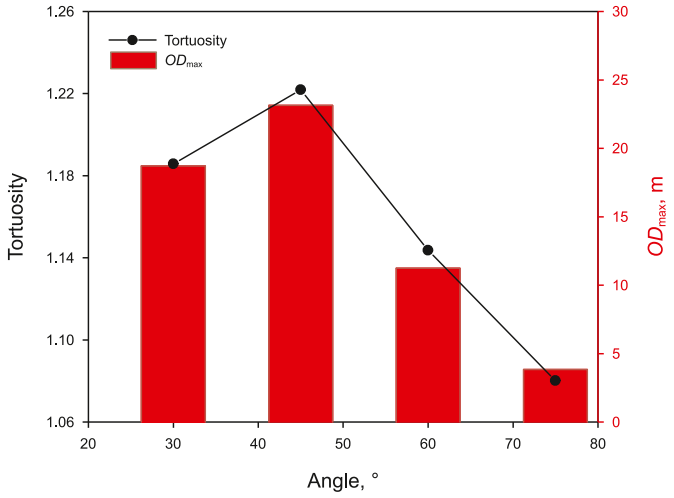

Fig. 20. Tortuosity and OD_{max} of HF at different angles of NFs.

interference, strong interference and weak interference is presented from the heel to the toe of the HF.

Fig. 27(b) shows the propagation pattern of multi-cluster HFs when the α is 30°. Comparative analysis shows that, unlike the single HF, the inner HF2 does not propagate along the NFs and thus deviates from the original propagation direction under the stress interference from the outer HFs. The outer HF1 and HF3, on the other hand, shows different degrees of offset, with OD_{max} of 15.18 and −7.62 m. The location of the OD_{max} of HF3 is not near the end but in the middle (at a propagation distance of about 56 m) of the HF. HF1 deflects to the outside under the action of stress interference between fractures, and the direction of its deflection is in good agreement with the direction of the NFs. In this case, the presence of NFs increases the degree of deflection of the outer HF. In contrast, the direction of outer HF3 under the action of inter-fracture stress interference is opposite to that of NFs, which makes the presence of the NFs inhibits the deflection of the outer HF. It is also noteworthy that the HFs still exhibit no interference, strong interference and weak interference from the heel to the toe. When HF3 is in a state of strong inter-fracture interference, it clearly shows a tendency to deflect to the outer side. As the HF continues to propagate, the degree of inter-fracture interference is not enough to resist the guiding effect of the NFs, which causes the HF to gradually deflect to the inner side instead. When the gap between the propagation distance of the inner HF and the outer HFs reaches a certain value, the HFs are in a weak interference state. In addition, in the absence of NFs, due to the friction resistance of the wellbore, the HF1 near the injection eventually leads to a longer propagation distance than

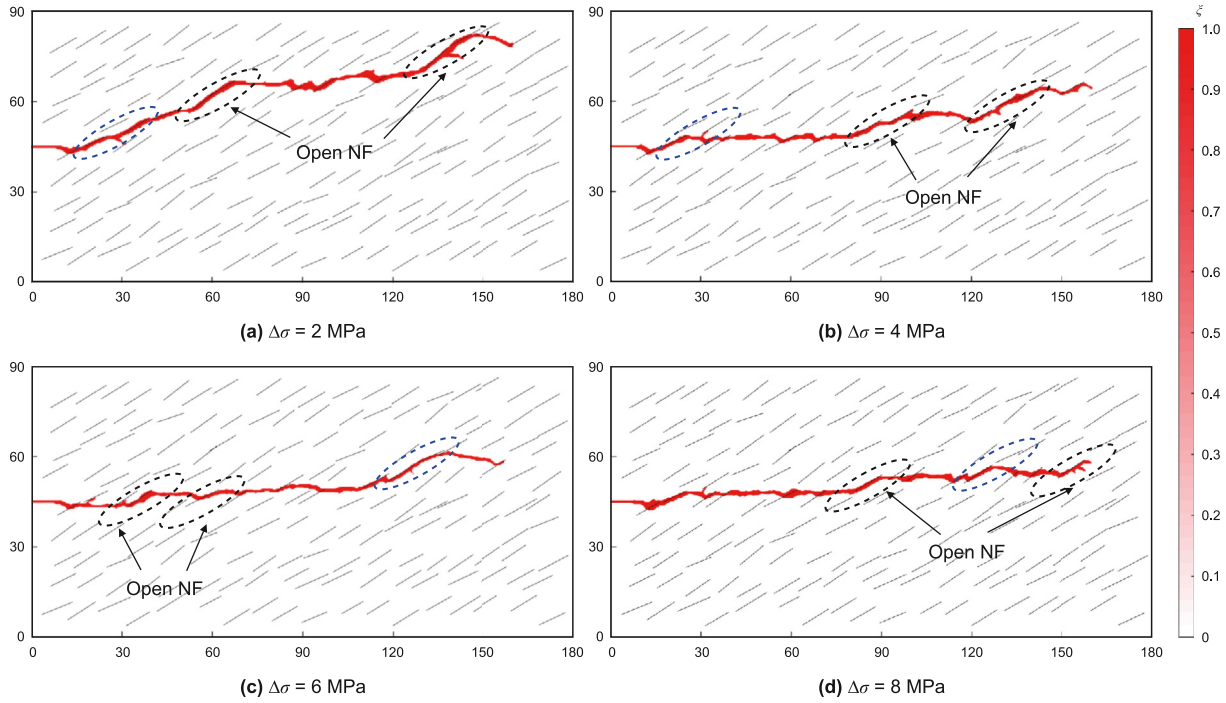

Fig. 21. The results of HF propagation at different stress differences.

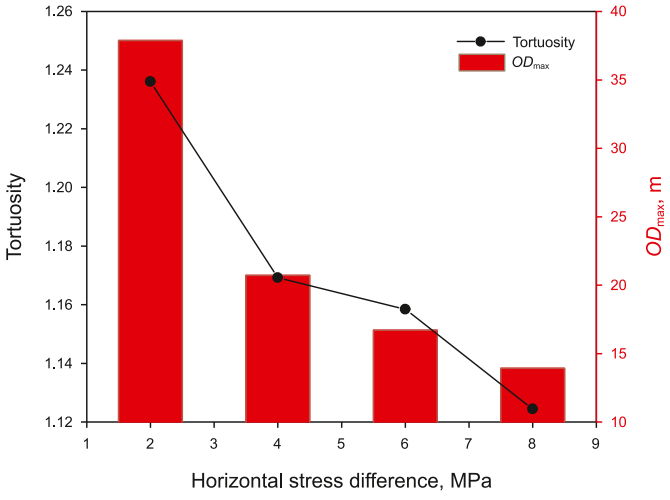

Fig. 22. Tortuosity and OD_{max} of HF at different stress differences.

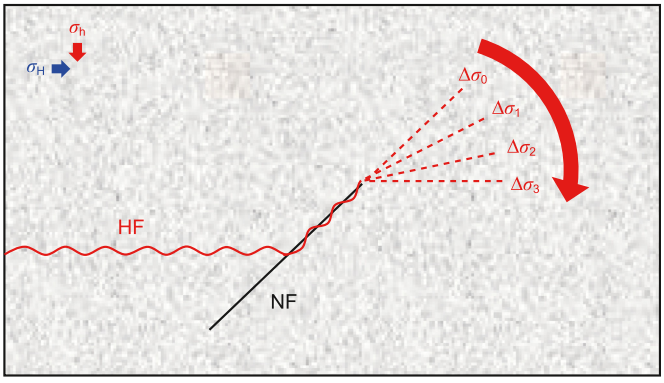

Fig. 23. The relationship between horizontal stress difference and deflection angle.

HF3. In the presence of NFs, the opposite trend is observed. This is due to the fact that the HF3 with a smaller offset propagates farther in the same time period, making the HF3 become the dominant fracture instead, which further leads to the HF3 propagating farther than the HF1 near the injection.

Fig. 28 shows the comparison between the injection rate of each fracture during the multi-cluster hydraulic fracturing process. The dynamic distribution results of the flow can also reflect that the HFs show the phenomenon of no interference, strong interference and weak interference in the propagation process. In the no interference stage, the fluid injection rate of each cluster of fractures is almost the same. In the strong interference stage, the initiation and propagation pressure of the inner HF2 increases under the effect of stress shadow, leading to a sharp decrease in its fluid injection rate. Since the total injection rate is certain, the fluid intake of the outer HF1 and HF3 instead increases sharply. There is a small wellbore friction between HF1 and HF3, so there is a small difference between the fluid intake of the two fractures. Until the HFs propagate to the weak interference zone, the fluid intake of each HF gradually stabilizes again. The trend of this simulation result is basically consistent with the findings of Wu and Olson (2016). Comparing the results of flow distribution with and without NFs, it can be seen that the fluctuation of flow distribution is larger under the influence of NFs. This is mainly due to the fact that when the HF propagates along the NF, the resistance to its propagation is smaller. Meanwhile, comparing the flow results of HF1 and HF3 in the presence of NFs, it can be seen that under the influence of wellbore friction, the fluid intake of HF1 in the early stage of propagation is larger than that of HF3. In the middle of propagation, HF3, which propagates farther, converts this disadvantage. Overall, due to the greater fluid intake of HF3, it eventually led to the fact that HF3 far from the injection became an advantageous fracture instead.

Angle of NFs. The angle of NFs is an important factor influencing the interaction between HF and NF, and Fig. 29 reveals the propagation patterns of multi-cluster HFs under different NF angles. When the α are 30°, 45°, and 60°, HF3 away from the injection

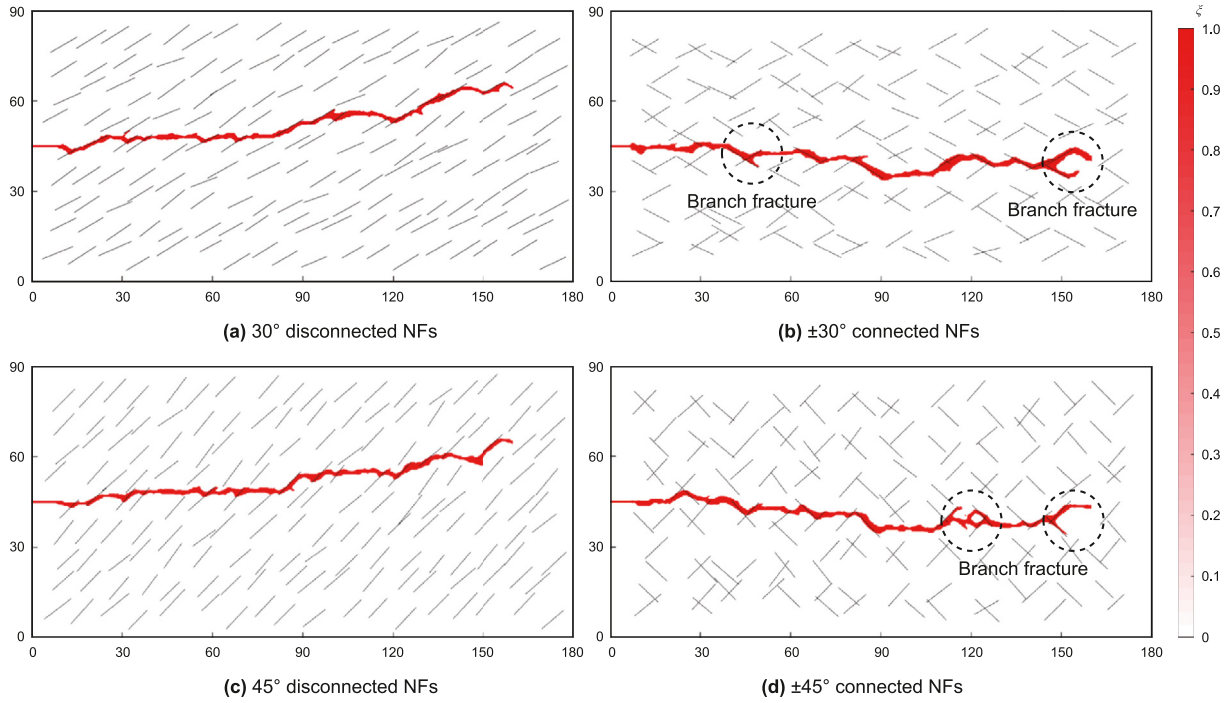

Fig. 24. The results of HF propagation at different states of NFs.

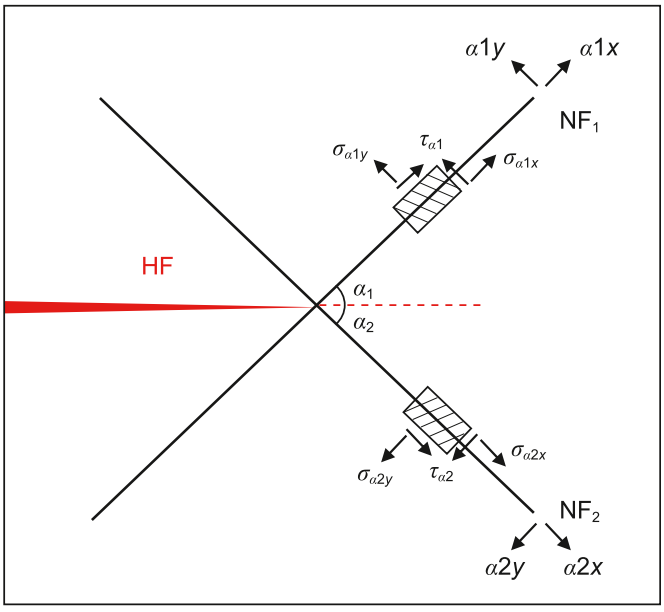

Fig. 25. Propagation analysis of HF at the intersection of connected NFs.

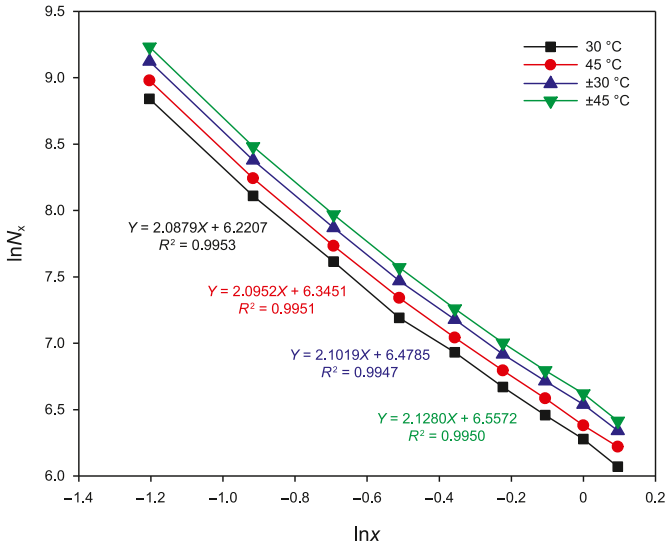

Fig. 26. Fractal dimension of HF at different states of NFs.

becomes the dominant fracture with the propagation extension distance under the common influence of inter-fracture stress interference and the guiding effect of NF clusters. When the α is 75°, the influence of NF clusters on HF propagation becomes minimal, stress interference becomes the main factor influencing HF propagation, and HF1 near the injection becomes the dominant fracture again. When the α is 30°, the NF has a better diverting performance for the HF under this condition. With the increasing angle of the NFs, this diverting ability gradually decreases. When the α is 75°, the OD_{max} of HF1 and HF3 are 9.94 and −9.32 m, respectively, which are very close to the deflection degree of HFs without NF clusters. At low NF angle (30° and 45°), the OD_{max} occurs in the middle of the HF, while at high NF angle (60° and 75°), the OD_{max} occurs at the end of the HF. In order to facilitate the analysis, the offset distance (OD) at the end of the HF was selected as a parameter.

Fig. 30 depicts the offset magnitude of HF1 and HF3 and the average tortuosity of HF at NF different angles. As can be seen from the figure, the OD_{max} of HF1 and HF3 show a decreasing and increasing trend with increasing NF angle, respectively. The end of HF3 gradually shows a tendency to be offset to the outside with the increase of NF angle. The area between the end offset curve and the OD_{max} curve represents the diverting performance of the NF in contrast to the stress interference on the multi-cluster HFs.

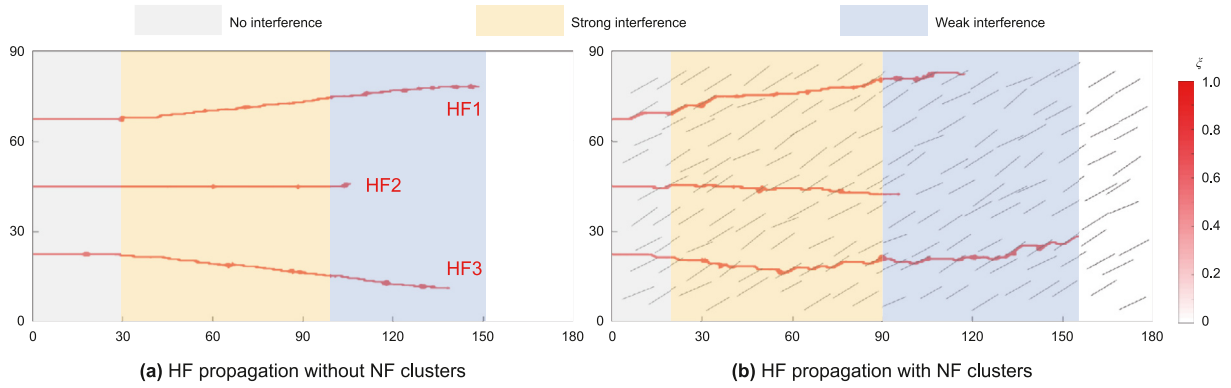

Fig. 27. Propagation patterns of multi-cluster HFs.

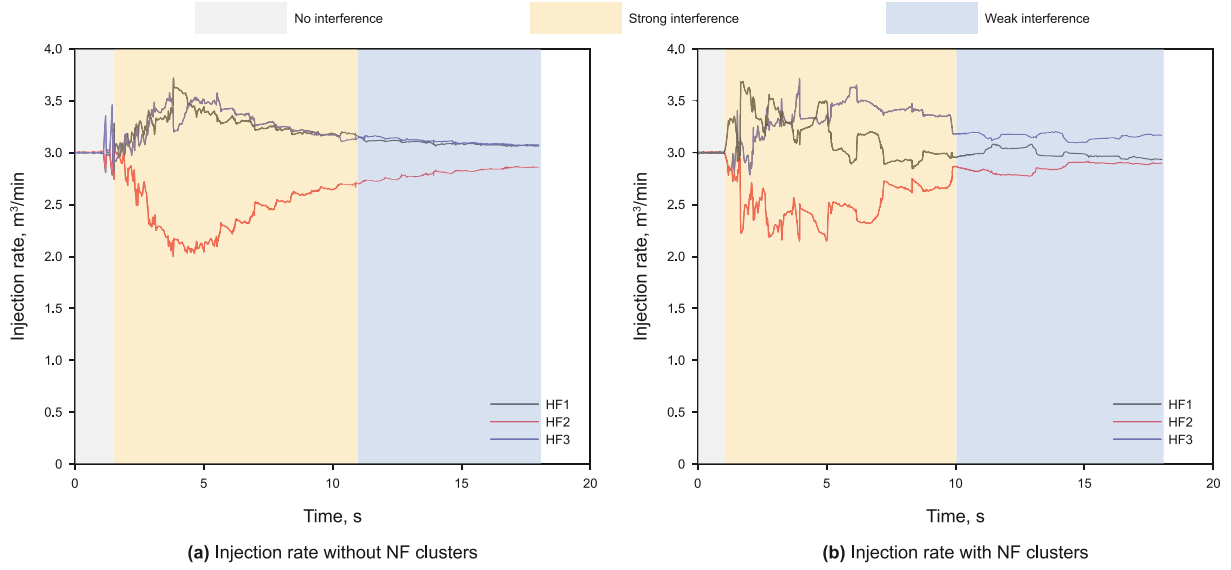

Fig. 28. Dynamic distribution of flow between fractures in multi-cluster hydraulic fracturing.

Meanwhile, based on the offset magnitude, it can be seen that HF3, which is offset in the opposite direction to the NF, is more sensitive than HF1, which is offset in a direction similar to the natural fracture. This is because the ability of NFs to offset HF is much stronger than the ability of inter-fracture interference to offset HF. When the direction of deflection under stress disturbance is opposite to the direction of NFs, the guiding ability of NFs is hostile to inter-fracture interference. When the effect of NFs is weakened, the inter-fracture interference will completely dominate the deflection of HFs. On the contrary, the guiding ability of NFs and inter-fracture interference are synergistic. Overall, the tortuosity of HFs under this condition shows a decreasing trend with the increase of angle. The difference in simulation results between a single HF and a NF clusters is due to the horizontal stress difference of 6 MPa and the effect of inter-fracture stress interference in this simulation. Meanwhile, the conclusion that the OD_{max} shows a strong correlation with tortuosity in the case of unconnected fractures still holds. It should be noted that under the influence of wellbore friction and perforation friction, the propagation distance of HFs formed at fracture clusters near the injection is not the farthest, and NFs are also the main factors affecting the formation of dominant fractures.

Connected NFs. For a single HF, the presence of connected NFs can induce the HF to form branch fractures. Fig. 31 shows the results of HF propagation for multi-cluster HFs when the NFs are connected and disconnected. Since the two sets of NFs with opposite directions have a complementary effect on the HFs, HF1 near the injection continues to be the dominant fracture with the farthest propagation distance. Compared to unidirectional fractures, the *OD* of HF1 and HF3 were effectively suppressed and facilitated, respectively, in the case of connected fractures with two directions. This is because unidirectional unconnected NFs promote and inhibit HFs in the same and opposite directions, respectively. The connected fractures with two directions have both facilitating and inhibiting effects depending on the actual interaction of HF and NF, thus inhibiting the directional guidance of the unidirectional NFs on the HFs. At an angle of ±30° of the NF, the HFs under this condition have a stronger ability to open the NFs after contacting them, resulting in the formation of more branch fractures during HFs propagation. It is worth noting that branch fractures almost always propagate along the outer side due to the effect of inter-fracture interference. This is because the stress shadow caused by the inner compression zone is strong, which inhibits the initiation and propagation of the inner branch fractures, while the initiation and propagation of the outer branch fractures are relatively easier, resulting in the formation of branch fractures almost located on the outside. Combined with Fig. 6, it can be seen that when the stress difference and approach angle are 6 MPa and ±45°, respectively, the condition is located near the criterion. Under the effect of stress

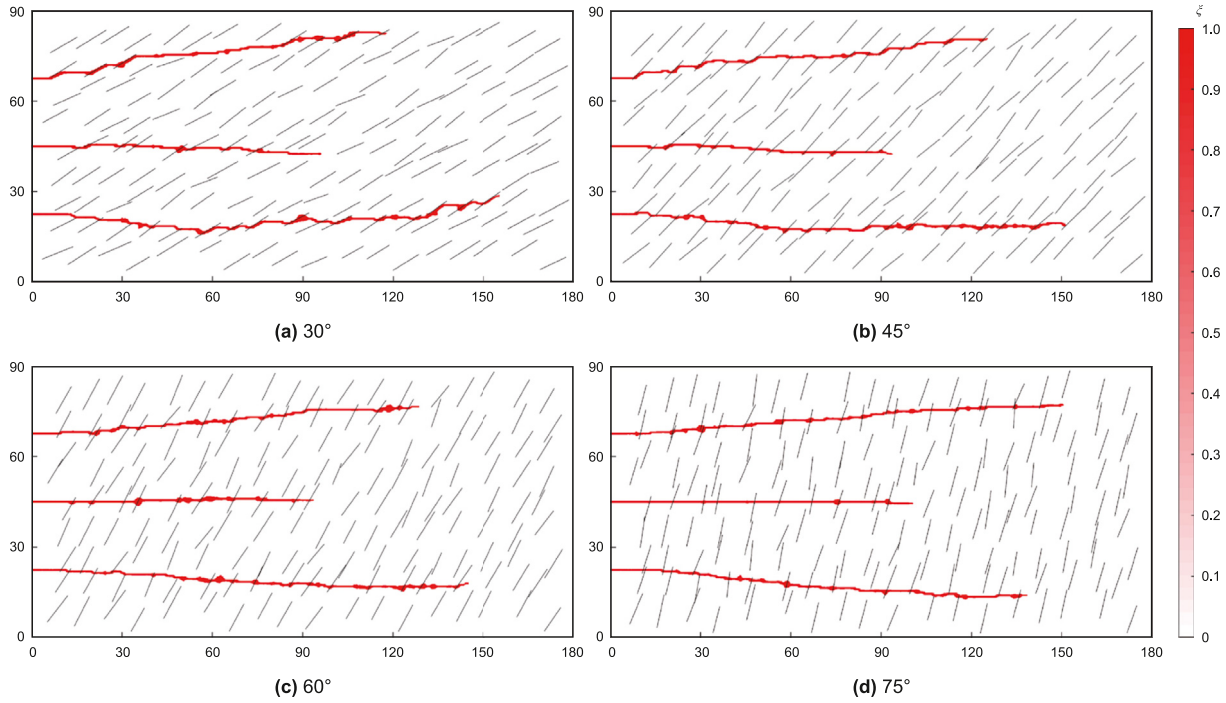

Fig. 29. Propagation patterns of multi-cluster HFs with different NF angles.

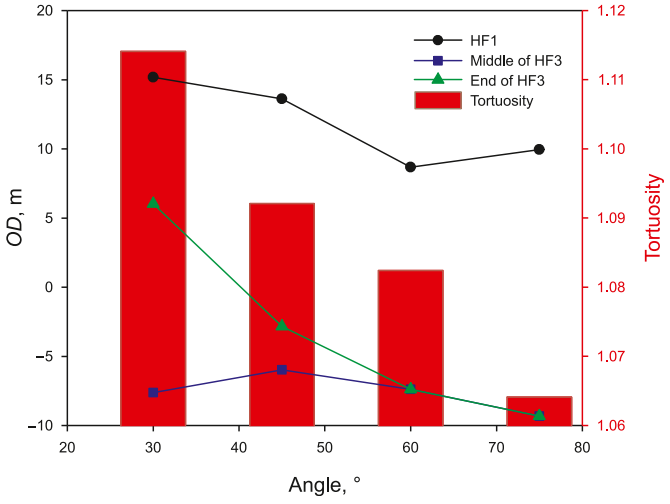

Fig. 30. *OD* of outer HFs and tortuosity under the combined effect of NFs and stress interference.

shadow, there are almost no branch fractures formed in HFs, and the propagation and offset of the HFs are mainly affected by inter-fracture stress interference. In other words, under the influence of stress shadow, the interaction pattern between multi-cluster HFs and NFs is more complex than that between single HF and NFs.

The fractal dimension of multi-cluster HFs under different NFs connection states is calculated in Fig. 32. From the simulation results, it can be seen that the HFs have the lowest complexity when the α is $\pm45°$, and the fractal dimension is 1.9932. This is because the diverting performance of the NFs on the HFs is weaker at this stress difference and approach angle. Relative to the α of 45°, although the linear densities of the NFs are all 0.1, the connected NFs make the distribution of the NFs produce a certain degree of agglomeration, resulting in the overall poor dispersion of the NFs in the reservoir. Meanwhile, the complementary effect of different sets of NFs in the connected NFs reduces the offset amplitude of HFs. These two reasons together lead to the complexity of the connected NFs being rather lower than the discrete NFs. The highest complexity of HFs was observed for NFs with α of $\pm30°$, which had a fractal dimension of 2.0523. This is mainly due to the fact that this approach angle and the horizontal stress difference located in the open zone are capable of causing the HFs to form branch fractures thus significantly increasing the HFs complexity. In addition to this, comparing the results of single HF with NF clusters, it can be seen that the fractal dimension of multi-cluster HFs is generally lower than that of single HF under the suppression effect of inter-fracture interference.

In summary, for multi-cluster HFs, the ability of connected NFs to increase the complexity of HFs is not necessarily stronger than that of disconnected NFs, which is related to stress difference and approach angle. Under the condition of the same NF density disconnected fractures have better dispersion and can help to enhance the complexity of HFs. When the approach angle and the horizontal stress difference are located in the cross zone or near the criterion, the presence of stress shadows makes HFs hardly form branch fractures. When the approach angle and horizontal stress difference are located in the open zone, the NFs can help the HFs to form branch fractures., which can further enhance the complexity of the HFs.

4. Conclusions

In this study, the HMD coupling HF propagation model is established using the phase field method. This model considers the dynamic distribution of flow between perforation clusters and the inter-fracture interference during the fracturing process. The propagation mechanism of HFs under single HF and single NF, reservoir heterogeneity, single HF and NF clusters, multi-cluster HF and NF clusters are investigated. Corresponding conclusions are obtained.

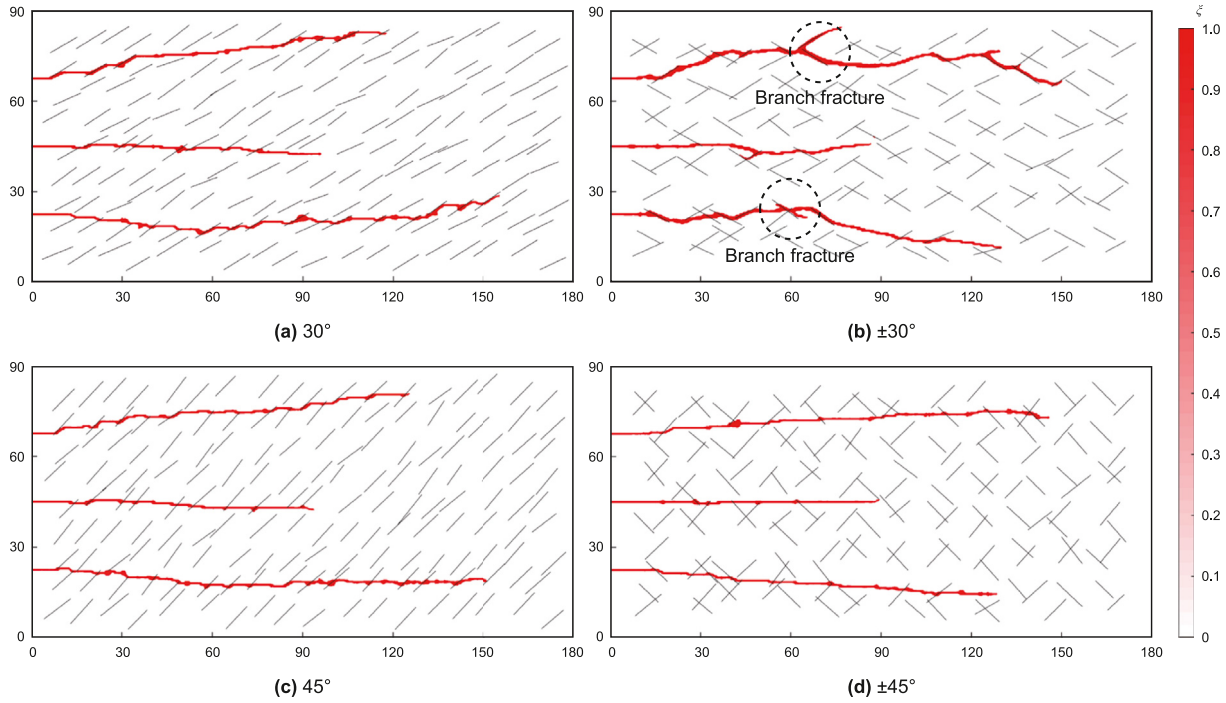

Fig. 31. The results of propagation of multi-cluster HFs at different states of NFs.

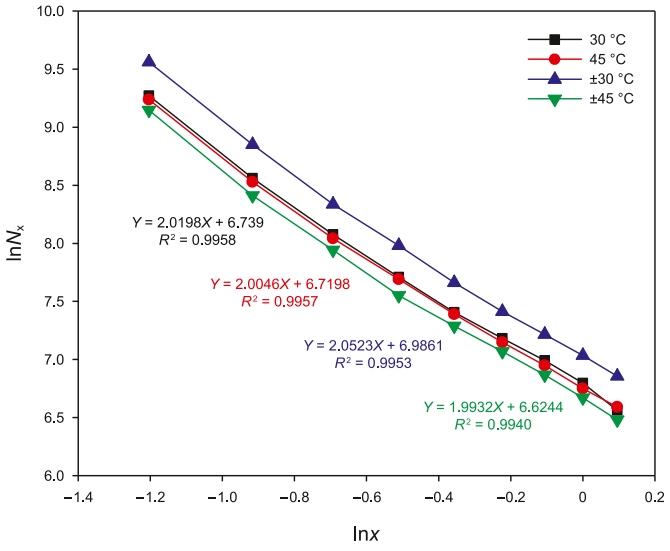

Fig. 32. Fractal dimensions of multi-cluster HFs at different states of NFs.

(1) The HMD coupling model in this study can accurately simulate the influence of approach angle, stress difference and cementation strength on the interaction mode of HF and NF. The criterion in the open area and the cross area are not fixed but gradually move to the lower left with the increase of cementation strength.

(2) The reservoir heterogeneity is an important parameter affecting the tortuosity of HF. When the reservoir shape parameter $m = 5$, even without the presence of NF, the tortuosity of HF can reach 1.08.

(3) The greater the density of NFs and the smaller the horizontal stress difference, the better the diverting performance of the NFs on HF. With the increase of NF angle, the main interaction between HF and NFs gradually changes from open to open and cross, and finally to cross. The NF angle is not a decisive parameter to discriminate the interaction. According to the relationship between the approach angle and the NF angle, the contact relationship of HF can be divided into three categories ($\alpha = \theta$, $\alpha < \theta$ and $\alpha > \theta$).

(4) The conclusion that OD_{max} shows a strong correlation with tortuosity does not apply to connected NF. The connected NF can increase the complexity of HF by inducing it to form branch fractures. Within a certain range, larger NF angles can increase the complexity of HF. At an angle of ±45°, the fractal dimension is 2.1280.

(5) The inter-fracture interference shows no, strong and weak interference from the heel to the toe of the HF and mainly acts on the outer HFs. This leads to the fact that at low angles, the location where the OD_{max} from the HF occurs is located in the middle of the HF. Under the action of NFs, even HFs far away from the injection can become the dominant fracture. With the gradual increase of the NF angle, the inter-fracture interference gradually becomes the main factor affecting HF propagation.

(6) Multi-cluster HFs are generally less complex than single HF due to the suppression of inter-fracture interference. When the approach angle and the horizontal stress difference are located in the crossing zone or neared criterion, the presence of stress shadows makes the HFs almost not form a branch fracture.

CRediT authorship contribution statement

Yun-Jin Wang: Writing – original draft, Software. **Bo Wang:** Visualization, Supervision. **Hang Su:** Methodology, Formal analysis. **Tu Chang:** Formal analysis. **Ren-Cheng Dong:** Methodology. **Li-Zhe Li:** Validation. **Wei-Yu Tang:** Validation. **Ting-Xue Jiang:** Supervision. **Fu-Jian Zhou:** Writing – review & editing, Supervision.

Declaration of competing interest

The authors declare that they have no known competing financial interests or personal relationships that could have appeared to influence the work reported in this paper.

Acknowledgment

This work is supported by the National Natural Science Foundation of China (No. 52174045).

References

Ambati, M., Gerasimov, T., De Lorenzis, L., 2015. A review on phase-field models of brittle fracture and a new fast hybrid formulation. Comput. Mech. 55, 383–405. https://doi.org/10.1007/s00466-014-1109-y.

Bahorich, B., Olson, J.E., Holder, J., 2012. Examining the effect of cemented natural fractures on hydraulic fracture propagation in hydrostone block experiments. In: SPE Annual Technical Conference and Exhibition. https://doi.org/10.2118/160197-MS.

Blanton, T., 1982. An experimental study of interaction between hydraulically induced and pre-existing fractures. In: SPE Unconventional Gas Recovery Symposium. https://doi.org/10.2118/10847-MS.

Dahi-Taleghani, A., Olson, J.E., 2011. Numerical modeling of multistranded-hydraulic-fracture propagation: accounting for the interaction between induced and natural fractures. SPE J. 16, 575–581. https://doi.org/10.2118/124884-PA.

Dong, J., Yuan, G., Wang, X., Chen, M., Jin, Y., Zeng, C., Zaman, M., 2021. Experimental study of multi-timescale crack blunting in hydraulic fracture. Petrol. Sci. 18, 234–244. https://doi.org/10.1007/s12182-020-00479-1.

Dong, R., Alpak, F.O., Wheeler, M.F., 2023. Accurate two-phase flow simulation in faulted reservoirs by combining two-point flux approximation and mimetic finite difference methods. SPE J. 28, 111–129. https://doi.org/10.2118/206298-PA.

Dong, S., Wang, L., Zeng, L., Du, X., Ji, C., Hao, J., Yang, X., Li, H., 2023. Fracture identification in reservoirs using well log data by window sliding recurrent neural network. Geoenergy Sci. Eng. 230, 212165. https://doi.org/10.1016/j.geoen.2023.212165.

Gu, H., Weng, X., 2010. Criterion for fractures crossing frictional interfaces at non-orthogonal angles. In: 44th U.S. Rock Mechanics Symposium and 5th U.S.-Canada Rock Mechanics Symposium.

Gu, H., Weng, X., Lund, J., Mack, M., Ganguly, U., Suarez-Rivera, R., 2012. Hydraulic fracture crossing natural fracture at nonorthogonal angles: a criterion and its validation. SPE Prod. Oper. 27, 20–26. https://doi.org/10.2118/139984-PA.

Guo, J., Zhao, X., Zhu, H., Zhang, X., Pan, R., 2015. Numerical simulation of interaction of hydraulic fracture and natural fracture based on the cohesive zone finite element method. J. Nat. Gas Sci. Eng. 25, 180–188. https://doi.org/10.1016/j.jngse.2015.05.008.

Guo, J., Lu, Q., Chen, H., Wang, Z., Tang, X., Chen, L., 2018. Quantitative phase field modeling of hydraulic fracture branching in heterogeneous formation under anisotropic in-situ stress. J. Nat. Gas Sci. Eng. 56, 455–471. https://doi.org/10.1016/j.jngse.2018.06.009.

Hofacker, M., Miehe, C., 2012. Continuum phase field modeling of dynamic fracture: variational principles and staggered FE implementation. Int. J. Fract. 178, 113–129. https://doi.org/10.1007/s10704-012-9753-8.

Hosseini, E., Sarmadivaleh, M., Chen, Z., 2021. Developing a new algorithm for numerical modeling of discrete fracture network (DFN) for anisotropic rock and percolation properties. J. Pet. Explor. Prod. Technol. 11, 839–856. https://doi.org/10.1007/s13202-020-01079-w.

Hu, X., Han, S., Ma, S., Zhou, F., Qiu, Y., Li, X., Li, M., Tu, Z., 2023. The influence of multi-metal-veins on fractures propagation investigated by the experiment and simulation. Petrol. Sci. 20 (3), 1707–1723. https://doi.org/10.1016/j.petsci.2022.11.009.

Huang, L., Tan, J., Fu, H., Liu, J., Chen, X., Liao, X., Wang, X., Wang, C., 2023. The non-plane initiation and propagation mechanism of multiple hydraulic fractures in tight reservoirs considering stress shadow effects. Eng. Fract. Mech. 292, 109570. https://doi.org/10.1016/j.engfracmech.2023.109570.

Jamaloei, B.Y., 2021. A critical review of common models in hydraulic-fracturing simulation: a practical guide for practitioners. Theor. Appl. Fract. Mech. 113, 102937. https://doi.org/10.1016/j.tafmec.2021.102937.

Jiang, J., Younis, R.M., 2016. Hybrid coupled discrete-fracture/matrix and multi-continuum models for unconventional-reservoir simulation. SPE J. 21, 1009–1027. https://doi.org/10.2118/178430-PA.

Lepillier, B., Yoshioka, K., Parisio, F., Bakker, R., Bruhn, D., 2020. Variational phase-field modeling of hydraulic fracture interaction with natural fractures and application to enhanced geothermal systems. J. Geophys. Res. Solid Earth 125, e2020JB019856. https://doi.org/10.1029/2020JB019856.

Li, M., Hu, X., Zhou, F., Wang, B., Han, S., Huang, G., 2020. Three-dimensional numerical simulation of interaction of hydraulic fracture and natural fracture using the cohesive zone finite element method. In: SPE/AAPG/SEG Latin America Unconventional Resources Technology Conference. https://doi.org/10.15530/urtec-2020-1380.

Li, M., Zhou, F., Yuan, L., Chen, L., Hu, X., Huang, G., Han, S., 2021. Numerical modeling of multiple fractures competition propagation in the heterogeneous layered formation. Energy Rep. 7, 3737–3749. https://doi.org/10.1016/j.egyr.2021.06.061.

Li, M., Zhou, F., Wang, B., Hu, X., Wang, D., Zhuang, X., Han, S., Huang, G., 2022. Numerical simulation on the multiple planar fracture propagation with perforation plugging in horizontal wells. Petrol. Sci. 19, 2253–2267. https://doi.org/10.1016/j.petsci.2022.05.004.

Li, N., Zhang, S., Zou, Y., Ma, X., Wu, S., Zhang, Y., 2018. Experimental analysis of hydraulic fracture growth and acoustic emission response in a layered formation. Rock Mech. Rock Eng. 51, 1047–1062. https://doi.org/10.1007/s00603-017-1383-z.

Liu, Y., Zhang, J., Bai, J., Zhang, F., Tang, J., 2023. Numerical study of hydraulic fracturing in the sectorial well-factory considering well interference and stress shadowing. Petrol. Sci. 20 (6), 3567–3581. https://doi.org/10.1016/j.petsci.2023.05.020.

Mack, M.G., Elbel, J.L., Piggott, A.R., 1992. Numerical representation of multilayer hydraulic fracturing. In: The 33rd U.S. Symposium on Rock Mechanics (USRMS).

Miehe, C., Hofacker, M., Welschinger, F., 2010. A phase field model for rate-independent crack propagation: robust algorithmic implementation based on operator splits. Comput. Methods Appl. Mech. Eng. 199, 2765–2778. https://doi.org/10.1016/j.cma.2010.04.011.

Peng, Y., Zhao, J., Sepehrnoori, K., Li, Y., Yu, W., Zeng, J., 2019. Study of the heat transfer in the wellbore during acid/hydraulic fracturing using a semianalytical transient model. SPE J. 24, 877–890. https://doi.org/10.2118/194206-PA.

Peng, Y., Luo, A., Li, Y., Wu, Y., Xu, W., Sepehrnoori, K., 2023. Fractional model for simulating long-term fracture conductivity decay of shale gas and its influences on the well production. Fuel 351, 129052. https://doi.org/10.1016/j.fuel.2023.129052.

Renshaw, C.E., Pollard, D.D., 1995. An experimentally verified criterion for propagation across unbounded frictional interfaces in brittle, linear elastic materials. Int. J. Rock Mech. Min. Sci. Geomech. Abstracts 32, 237–249. https://doi.org/10.1016/0148-9062(94)00037-4.

Shiozawa, S., Lee, S., Wheeler, M.F., 2019. The effect of stress boundary conditions on fluid-driven fracture propagation in porous media using a phase-field modeling approach. Int. J. Numer. Anal. Methods GeoMech. 43, 1316–1340. https://doi.org/10.1002/nag.2899.

Siriwardane, H.J., Layne, A.W., 1991. Improved model for predicting multiple hydraulic fracture propagation from a horizontal well. In: SPE Eastern Regional Meeting. https://doi.org/10.2118/23448-MS.

Su, H., Zhou, F., Zheng, A., Wang, L., Wang, C., Yu, F., Kang, L., Li, J., 2022. Heavy oil recovery by alkaline-cosolvent-polymer flood: a multiscale research using micromodels and computed tomography imaging. SPE J. 27 (3), 1480–1492. https://doi.org/10.2118/204766-PA.

Tan, P., Jin, Y., Yuan, L., Xiong, Z., Hou, B., Chen, M., Wan, L., 2019. Understanding hydraulic fracture propagation behavior in tight sandstone–coal interbedded formations: an experimental investigation. Petrol. Sci. 16, 148–160. https://doi.org/10.1007/s12182-018-0297-z.

Tang, W., Sheng, J., 2022. Huff-n-puff gas injection or gas flooding in tight oil reservoirs? J. Petrol. Sci. Eng. 208, 109725. https://doi.org/10.1016/j.petrol.2021.109725.

Tang, W., Sheng, J., Jiang, T., 2023. Further discussion of CO_2 huff-n-puff mechanisms in tight oil reservoirs based on NMR monitored fluids spatial distributions. Petrol. Sci. 20 (1), 350–361. https://doi.org/10.1016/j.petsci.2022.08.014.

Wang, J., Xie, H., Matthai, S.K., Hu, J., Li, C., 2023. The role of natural fracture activation in hydraulic fracturing for deep unconventional geo-energy reservoir stimulation. Petrol. Sci. 20 (4), 2141–2164. https://doi.org/10.1016/j.petsci.2023.01.007.

Wang, L., Mou, J., Mo, S., Zhao, B., Liu, Z., Tian, X., 2020. Modeling matrix acidizing in naturally fractured carbonate reservoirs. J. Petrol. Sci. Eng. 186, 106685. https://doi.org/10.1016/j.petrol.2019.106685.

Wang, Y., Zhou, F., Su, H., Li, Y., Yu, F., Dong, R., Wang, Q., Li, J., 2023a. Performance evaluation of microemulsion acid for integrated acid fracturing in Middle Eastern carbonate reservoirs. Petrol. Explor. Dev. 50, 1196–1205. https://doi.org/10.1016/S1876-3804(23)60458-6.

Wang, Y., Zhou, F., Zhang, Y., Su, H., Dong, E., Bai, H., Wang, B., Wang, Q., Dong, R., 2023b. The influence of fracture surface morphology on nonuniform etching in limestone acid fracturing. Geoenergy Sci. Eng. 230, 212234. https://doi.org/10.1016/j.geoen.2023.212234.

Wang, Y., Zhou, F., Zhang, Y., Wang, Yaocong, Su, H., Dong, R., Wang, Q., Bai, H., 2023c. Numerical studies and analysis on reaction characteristics of limestone and dolomite in carbonate matrix acidizing. Geoenergy Sci. Eng. 222, 211452. https://doi.org/10.1016/j.geoen.2023.211452.

Warpinski, N.R., Teufel, L.W., 1987. Influence of geologic discontinuities on hydraulic fracture propagation (includes associated papers 17011 and 17074). J. Petrol. Technol. 39, 209–220. https://doi.org/10.2118/13224-PA.

Wei, C., Zhu, W., Yu, Q., Xu, T., Jeon, S., 2015. Numerical simulation of excavation damaged zone under coupled thermal–mechanical conditions with varying mechanical parameters. Int. J. Rock Mech. Min. Sci. 75, 169–181. https://doi.org/10.1016/j.ijrmms.2014.11.010.

Wu, K., Olson, J.E., 2014. Simultaneous multifracture treatments: fully coupled fluid flow and fracture mechanics for horizontal wells. SPE J. 20, 337–346. https://doi.org/10.2118/167626-PA.

Wu, K., Olson, J.E., 2016. Mechanisms of simultaneous hydraulic-fracture

propagation from multiple perforation clusters in horizontal wells. SPE J. 21, 1000–1008. https://doi.org/10.2118/178925-PA.
Xu, H., Li, Y., Zhou, F., Su, H., Yao, E., Hu, J., Chen, Z., 2023. Adsorption characteristics, isotherm, kinetics, and diffusion of nanoemulsion in tight sandstone reservoir. Chem. Eng. J. 470, 144070. https://doi.org/10.1016/j.cej.2023.144070.
You, J., Lee, K.J., 2021. A pore–scale investigation of surface roughness on the evolution of natural fractures during acid dissolution using DBS method. J. Petrol. Sci. Eng. 204, 108728. https://doi.org/10.1016/j.petrol.2021.108728.
Zhang, B., Guo, T., Qu, Z., Wang, J., Chen, M., Liu, X., 2023a. Numerical simulation of fracture propagation and production performance in a fractured geothermal reservoir using a 2D FEM-based THMD coupling model. Energy 273, 127175. https://doi.org/10.1016/j.energy.2023.127175.
Zhang, B., Qu, Z., Guo, T., Chen, M., Jiwei, W., Zhang, Y., 2023b. Numerical simulation on hydraulic fracture propagation in laminated shale based on thermo-hydro-mechanical-damage coupling model. Int. J. Damage Mech. 32, 105678952311608. https://doi.org/10.1177/10567895231160812.
Zhou, J., Chen, M., Jin, Y., Zhang, G., 2008. Analysis of fracture propagation behavior and fracture geometry using a tri-axial fracturing system in naturally fractured reservoirs. Int. J. Rock Mech. Min. Sci. 45, 1143–1152. https://doi.org/10.1016/j.ijrmms.2008.01.001.
Zhou, S., Zhuang, X., Rabczuk, T., 2018. A phase-field modeling approach of fracture propagation in poroelastic media. Eng. Geol. 240, 189–203. https://doi.org/10.1016/j.enggeo.2018.04.008.
Zhou, S., Zhuang, X., Rabczuk, T., 2020. Phase field method for quasi-static hydro-fracture in porous media under stress boundary condition considering the effect of initial stress field. Theor. Appl. Fract. Mech. 107, 102523. https://doi.org/10.1016/j.tafmec.2020.102523.
Zhuang, X., Zhou, S., Sheng, M., Li, G., 2020. On the hydraulic fracturing in naturally-layered porous media using the phase field method. Eng. Geol. 266, 105306. https://doi.org/10.1016/j.enggeo.2019.105306.
Zou, J., Zhang, Y., Zhang, L., Jing, J., Fu, Y., Wang, Y., Zhang, G., Zhou, F., 2023. Numerical simulation research on the effect of artificial barrier properties on fracture height. Processes 11, 310. https://doi.org/10.3390/pr11020310.
Zou, Y., Ma, X., Zhang, S., Zhou, T., Li, H., 2016a. Numerical investigation into the influence of bedding plane on hydraulic fracture network propagation in shale formations. Rock Mech. Rock Eng. 49, 3597–3614. https://doi.org/10.1007/s00603-016-1001-5.
Zou, Y., Zhang, S., Ma, X., Zhou, T., Zeng, B., 2016b. Numerical investigation of hydraulic fracture network propagation in naturally fractured shale formations. J. Struct. Geol. 84, 1–13. https://doi.org/10.1016/j.jsg.2016.01.004.
Zou, Y., Zhang, S., Zhou, T., Zhou, X., Guo, T., 2016c. Experimental investigation into hydraulic fracture network propagation in gas shales using CT scanning technology. Rock Mech. Rock Eng. 49, 33–45. https://doi.org/10.1007/s00603-015-0720-3.
Zou, Y., Ma, X., Zhang, S., 2020. Numerical modeling of fracture propagation during temporary-plugging fracturing. SPE J. 25, 1503–1522. https://doi.org/10.2118/199351-PA.